Infragravity Waves Across a Steeper-Sloping Rough Rocky Seabed on the Inner Shelf

Jamie MacMahan[1], Falk Feddersen[2], Ad JHM Reniers[3], Edward B Thornton[1,4], Olavo B Marques[1,2,5]

[1]Oceanography Department, Naval Postgraduate School, Monterey, CA, USA
[2]Scripps Institution of Oceanography, University of California, San Diego, CA, USA
[3]Civil Engineering and Geosciences, Delft University of Technology, Delft, Netherlands
[4]Moss Landing Marine Laboratories, University of California, San Jose, CA, USA
[5]Oregon State University, Corvallis, OR, USA

Key Points:

- Rocky shore infragravity waves are predominantly free, progressive, and follow linear dispersion with O(10%) bound wave contribution
- Nonlinear energy transfer drives the cross-shore flux gradient, balanced by bottom dissipation from the rough rocky seabed
- Extended rocky shores reduce infragravity energy, limiting reflective and refracted wave contributions seen on sandy coasts

Corresponding author: Jamie MacMahan, `jhmacmah@nps.edu`

Abstract

Field observations of infragravity (IG) waves were conducted from June to October 2023 along the steeper sloping (1:40) rocky shores off China Rock, CA, on the inner shelf at depths of 8 to 13 meters. The study examines the behavior of IG waves on the inner shelf, emphasizing the influence of a rough seabed and steeper slopes, and compares results with those from sandy shores and coral reefs, which have smoother seabeds and gentler slopes. IG energy correlated with sea-swell (SS) energy but exhibited a flat spectral distribution across the IG frequency band, showing minimal variation with tides or storms. Cross-spectral phase analysis revealed a constant progressive IG wave structure. Theoretical spectral phase computations based on linear dispersion compare well with observations, suggesting that IG waves are free, further supported by bispectral analysis estimating approximately 90% of the IG energy to be free. These findings contrast with sandy shores, where standing waves typically produce frequency-dependent nodal structures. A cross-shore energy flux balance indicated that nonlinear energy transfer dominated the IG energy flux gradient. Excess energy is balanced by bottom dissipation over the rough seabed, with friction factors larger than, though comparable to, coral reef flats. Relative IG-to-SS energy was lower than in other environments, likely due to the absence of reflected and refractively trapped waves along the extended stretch of rocky shores. These findings suggest that IG waves in this region are locally generated, propagate freely shoreward as a progressive wave, and are dissipated by the rough rocky seabed.

Plain Language Summary

Seventy-five percent of the world's coastlines are rocky; however, most wave and current research has focused on sandy shores and coral reefs. Rocky shores feature much rougher seabeds and steeper slopes, which can significantly influence nearshore wave and current dynamics. This study examines the impact of these conditions on long-period (25–200 s) infragravity (IG) waves, which dominate shallow-water hydrodynamics along many coastlines. Field observations off China Rock, Pebble Beach, on the outer Monterey Peninsula in California, on the inner shelf reveal IG wave behavior distinct from that observed on sandy shores. Instead of forming standing wave patterns due to shoreline reflection, the IG waves observed are progressive, freely propagating with a linear dispersion relationship. Unlike other environments, the coupling between IG waves and incident swell groups appears minimal in this case. Nonlinear triad interactions and bottom dissipation play key roles in the cross-shore energy flux balance of IG waves over rocky substrates, consistent with similar findings regarding sea-swell (SS) waves. The relative energy of IG waves compared to SS waves is lower than that on sandy shores or coral reefs, likely because reflected and refractively-trapped IG waves, common on sandy beaches, are absent along this extended stretch of rocky coast.

1 Introduction

Infragravity (IG) waves (periods of 25–200 s, 0.005–0.04 Hz) recorded on rocky shores are compared to previous field observations from sandy shores and coral reefs. Approximately 75% of the world's coastlines are classified as rocky, as estimated by Bird (2011). Rocky coasts can be further divided into rough, rocky seabeds extending across subtidal and intertidal zones, as well as rocky platforms. This study primarily focuses on rough, rocky shores, where the rugged seabed extends offshore from the shoreline. Rocky shores typically feature rougher seabeds (vertical standard deviation, σ_z, ranging from 0.35 to 9 m) compared to coral reefs ($\sigma_z = 0.1$ to 1 m) (e.g., MacMahan et al., 2024). Uneven, rough seabeds, either rocky or coral, have been shown to influence sea-swell (SS) waves in the inner shelf (e.g., Monismith et al., 2015; Gon et al., 2020; Marques et al., 2024; Marques, Feddersen, MacMahan, Acevedo-Ramirez, & Suanda, 2025) and in shallow bays (e.g., Mulligan et al., 2010), surf zone and inner shelf currents (e.g., MacMahan et al., 2023; Amador et al., 2020; Quinn et al., 2025), and IG waves in shallow water ($<$ 6 m depths) (e.g., Pomeroy et al., 2012; Becker et al., 2016; Winter et al., 2017).

Like the abundance of rocky shores in the world, IG waves are a significant nearshore signal found ubiquitously on most sandy beaches (e.g., Huntley et al., 1981; Guza & Thornton, 1985; Elgar et al., 1992; Herbers, Elgar, & Guza, 1995) and coral reefs (e.g., Nakaza & Hino, 1991; Hardy & Young, 1996; Lugo-Fernandez et al., 1998; Brander et al., 2004; Pequignet et al., 2009; Pomeroy et al., 2012; Torres-Freyermuth et al., 2012; Pequignet et al., 2014; Becker et al., 2016), often surpassing SS waves in shallower depths, near the shoreline (e.g., Guza & Thornton, 1985; Ruessink, 1998; Pomeroy et al., 2012). They play a significant role in surf zone hydrodynamics (e.g. rip current pulsations, MacMahan et al., 2004) and are critical for sediment transport (Beach & Sternberg, 1988; Aagaard & Greenwood, 1994, 2008; de Bakker, Brinkkemper, et al., 2016) and morphodynamics (Reniers et al., 2004; Roelvink & Reniers, 2012), and contribute to seiche (Okihiro et al., 1993; MacMahan, 2015). See Bertin et al. (2018) for an overview of IG waves. Most of the IG-wave field observations were on sandy shores and focused on IG generation, cross-shore behavior, amplification, and dissipation (e.g., Suhayda, 1974; Huntley, 1976; Huntley et al., 1981; Oltman-Shay & Howd, 1993; Elgar et al., 1992; Herbers, Elgar, & Guza, 1995; Herbers, Elgar, Guza, & O'Reilly, 1995; Sheremet et al., 2002; Henderson et al., 2006; Thomson et al., 2006; Lange et al., 2024). IG waves on coral reefs are also well-studied in the field, where the IG signal is significant across the reef flats (e.g., Nakaza & Hino, 1991; Hardy & Young, 1996; Lugo-Fernandez et al., 1998; Brander et al., 2004; Pequignet et al., 2009; Pomeroy et al., 2012; Torres-Freyermuth et al., 2012; Pequignet et al., 2014; Becker et al., 2016). There are few field studies of IG waves on rocky shores. Most are conducted in shallow water, such as across a subaqueous headland-like reef (depths $<$ 6 m) (e.g., Winter et al., 2017), within surge channels located within rocky headland that extend well above the sea surface (depths $<$ 2 m) (e.g., MacMahan et al., 2023), or on rocky platforms within the intertidal zone (e.g., Poate et al., 2018, 2020).

Two types of forced IG waves exist on the inner shelf, seaward of the surf zone. The first are bound IG waves, generated by nonlinear interactions among SS waves. Bound IG waves do not follow the linear dispersion relation and propagate with the SS wave groups (Longuet-Higgins & Stewart, 1962; Hasselmann, 1962; Herbers, Elgar, & Guza, 1995; Herbers & Burton, 1997; Lange et al., 2024). The second are free IG waves, produced by nonlinear triad interactions involving SS and IG components. These waves do follow the linear dispersion relation and propagate independently (Herbers, Elgar, Guza, & O'Reilly, 1995; Herbers & Burton, 1997; Norheim et al., 1998; Smit et al., 2018; Lange et al., 2024).

As summarized by Herbers and Burton (1997), in dispersive finite-depth theory ($kh \gg 1$), triad interactions are typically nonresonant (Herbers & Burton, 1997; Norheim et al., 1998). Two primary SS waves that satisfy the linear dispersion relation can generate a secondary bound wave that travels with the group velocity of the SS envelope, remaining 180° out of phase with the forcing (Longuet-Higgins & Stewart, 1962; Hasselmann, 1962; Herbers, Elgar, & Guza, 1995). As the primary SS waves shoal ($kh = O(1)$), the dispersion mismatch of the bound wave decreases, amplifying its energy (Herbers & Burton, 1997). However, in shallow water ($kh \ll 1$), finite-depth theory becomes invalid when the SS interactions become resonant, resulting in unphysical predictions of infinite bound wave amplitude. In contrast, Boussinesq (triad) theory accounts for slight deviations from resonance through slow modulations of amplitude and phase, allowing continuous energy transfer to a freely propagating secondary wave. Boussinesq theory is applicable in shallow water ($kh \ll 1$) but becomes ineffective in deep water ($kh \gg 1$), where strong dispersion leads to rapid variations in wave properties (Herbers & Burton, 1997). The two theories overlap for small-amplitude waves on gently sloping beaches, allowing for a smooth transition ($kh = O(1)$) from nonresonantly forced bound waves in deeper water to resonantly forced free waves in shallower water.

Herbers and Burton (1997) and Norheim et al. (1998) numerically demonstrated that steep bottom slopes (e.g., 1:30) reduce nonlinear energy transfer by triad interactions. Similar findings were reported by de Bakker, Tissier, and Ruessink (2016), who showed that on a steep-sloping beach (1:20), SS wave energy dominates the motion across the entire profile. Herbers and Burton (1997) further noted that steep slopes can significantly influence the shoaling, mainly when depth changes occur over spatial scales comparable to the secondary wavelength. In such cases, the assumption of a slowly varying depth—central to both finite-depth and Boussinesq theories—breaks down, leading to notable discrepancies between the two approaches. As a result, Boussinesq (triad) theory predicts significantly reduced nonlinear energy transfer under steep slope conditions (Herbers & Burton, 1997; Norheim et al., 1998; de Bakker, Tissier, & Ruessink, 2016). Consequently, the dynamics of IG wave transformation over steep slopes remain uncertain, particularly with a lack of field observations in these scenarios, and require further investigation.

A significant amount of IG energy has been discovered to be free on the inner shelf for long reaches of sandy shores, which is crucial for the seaward boundary conditions for the inner shelf (e.g., Fiedler et al., 2019; Rijnsdorp et al., 2022; Lange et al., 2024). On sandy shores, bound wave energy is typically small, generally less than 30% of the total IG energy along the inner shelf (e.g., Elgar et al., 1992; Herbers et al., 1994; Ruessink, 1998; Lange et al., 2024), and increases significantly only during storm events (Reniers et al., 2021). The majority of free IG waves are typically associated with those generated during SS wave shoaling and breaking (e.g., Herbers & Burton, 1997; Norheim et al., 1998; Henderson & Bowen, 2002; Henderson et al., 2006; Thomson et al., 2006; Contardo et al., 2021), as well as being reflected offshore at the shoreline (e.g., Huntley et al., 1981; Guza & Thornton, 1985; Elgar et al., 1992; Baldock et al., 2000; Sheremet et al., 2002; de Bakker et al., 2014; Inch et al., 2017). With a significant portion of the reflected energy being refractively trapped (e.g., Herbers, Elgar, & Guza, 1995; Smit et al., 2018), this increases the relative contribution of free IG waves (e.g., Ardhuin et al., 2014; Lange et al., 2024). Free IG waves can also arrive from distant coasts (e.g., Ardhuin et al., 2014), although they are generally considered small (e.g., Herbers, Elgar, & Guza, 1995; Sheremet et al., 2002; Lange et al., 2024), unless in semi-enclosed basins, such as the North Sea (Reniers et al., 2021).

Most previous research on the cross-shore IG energy flux balance was concentrated in the surf zone, focusing on the loss of IG energy in this region (e.g., Henderson & Bowen, 2002; Thomson et al., 2006; de Bakker et al., 2014), due to nonlinear transfers back to SS waves (e.g., Thomson et al., 2006; Henderson et al., 2006), bottom friction (e.g., Henderson & Bowen, 2002; Pomeroy et al., 2012), and IG wave breaking (e.g., Battjes et al., 2004; Van Dongeren et al., 2007; de Bakker et al., 2014; MacMahan et al., 2023). On sandy shores, IG energy dissipation on the inner shelf outside of wave breaking is considered minimal, likely due to relatively small bottom friction factors for sand roughness, which have little effect on SS wave dissipation (e.g., Thornton & Guza, 1983; Thornton & MacMahan, 2024). In contrast, rocky shores exhibit bottom friction factors an order of magnitude larger because of their rougher seabeds, making bottom dissipation significant for SS waves on the inner shelf (e.g., Gon et al., 2020; Marques, Feddersen, MacMahan, Acevedo-Ramirez, & Suanda, 2025; Thornton & MacMahan, 2024) and therefore likely important for IG waves on the inner shelf.

Infragravity waves observed over several months from summer to fall along a steeper sloping (1:40) rough rocky shore on the inner shelf at China Rock, Pebble Beach, centrally located at the outer edge of the Monterey Peninsula, California, USA, are examined and discussed. The inner shelf is the region located between the surf zone, where depth-limited wave breaking happens, and the mid shelf, where the surface and bottom boundary layers no longer overlap (e.g., Austin & Lentz, 2002; Lentz & Fewings, 2012). The field experiment and instrumentation are detailed in Section 2.1. Previous field studies of IG waves on sandy beaches and coral reefs provide a statistical framework for examining observations from fixed stations on rocky shores (Section 2.2). The general statistical, temporal, and spatial patterns highlighting storm events and tidal signatures are first described in Section 3.1. IG waves are initially examined in Sections 3.2-3.3, focusing on their spectral characteristics, including spectral analysis of their phase relationships and propagation. IG energy estimates are discussed in Section 3.4, which includes contributions of bound and free IG energy computed from normalized bispectral analysis, as well as their corresponding biphases. A cross-shore IG energy flux balance is performed between instrument pairs, detailing contributions by nonlinear transfers balanced against bottom frictional dissipation (Section 4.1). Energy friction factors are calculated as a free parameter in the energy-flux balance, as described in Section 4.2. Finally, the lower relative IG-to-SS energy measured at China Rock is discussed in the context of other studies on sandy and rocky shores, as well as coral reefs (Section 4.3), with a conclusion provided in Section 5.

2 Methods

2.1 Experiment and Instrumentation

A field experiment was conducted from June 22 to October 30, 2023, along the outer edge of the Monterey Peninsula at the landmark location China Rock in Pebble Beach, California, USA (Figure 1). China Rock is centrally located between Cypress Point to the south and Point Pinos to the north, spanning approximately 8 km. This shoreline reach is predominantly composed of rocky shores. The experiment's duration encompasses multiple synoptic wave events typical of the summer and fall seasons, providing a strong IG temporal signal that spans several spring and neap tidal cycles. This work complements other studies in the region that examine the influence of a rough, rocky seabed on wave and circulation processes (Feddersen et al., 2024; Collins et al., 2024; Marques et al., 2024; Marques, Feddersen, MacMahan, Acevedo-Ramirez, & Suanda, 2025; Quinn et al., 2025), as part of the Rocky Shores Experiments and SImulations (ROXSI) five-year research effort.

The China Rock field site was selected because it primarily consists of rocky terrain (see Figure 2), where the rocky substrate rises above the high tide line at the shoreline, and the rough, rocky seabed reaches depths greater than 80 m approximately 4.2 km from the shore. The bathymetric and topographic elevation maps were sourced from integrated airborne water-penetrating LIDAR surveys, vessel-based multibeam surveys, and in-house bathymetric surveys with a single-beam survey system tailored for shallow-water rocky shores. For further details on the elevation survey, see Marques et al. (2024); Marques, Feddersen, MacMahan, Acevedo-Ramirez, and Suanda (2025). The map of elevation relative to mean sea level z_{msl} is presented in a local coordinate system with cross-shore x (negative is offshore and directed towards 285°N) and alongshore y (Figure 2a). The average vertical standard deviation, σ_{z}, for this reach of China Rock bathymetry was measured at 0.9 m (Marques et al., 2024; Marques, Feddersen, MacMahan, Acevedo-Ramirez, & Suanda, 2025), which indicates considerable variability in the rocky bathymetry at this site. The alongshore average profile z_{mean} is computed for $-325 < y < 325$ m, and the average bottom slope, with a ratio of 1:40, is steeper than typical sandy shores (Figure 2b). The alongshore variability relative to z_{mean} is shown in Figure 2b to emphasize the bed roughness, where the alongshore $\sigma_{\mathrm{z}}(x)$ remains relatively consistent at approximately 1 m throughout the cross-shore profile. The range of alongshore bathymetric extrema (i.e., alongshore maxima z_{max} minus the alongshore minima z_{min}) spans close to 10 m, further highlighting the significant subaqueous variability of the seabed.

The analysis focuses entirely on pressure measurements obtained from standalone, bottom-mounted pressure sensors that were continuously sampled at a rate of 1 Hz. These sensors were secured to small, weighted mounts (32 kg) placed along the rocky seabed

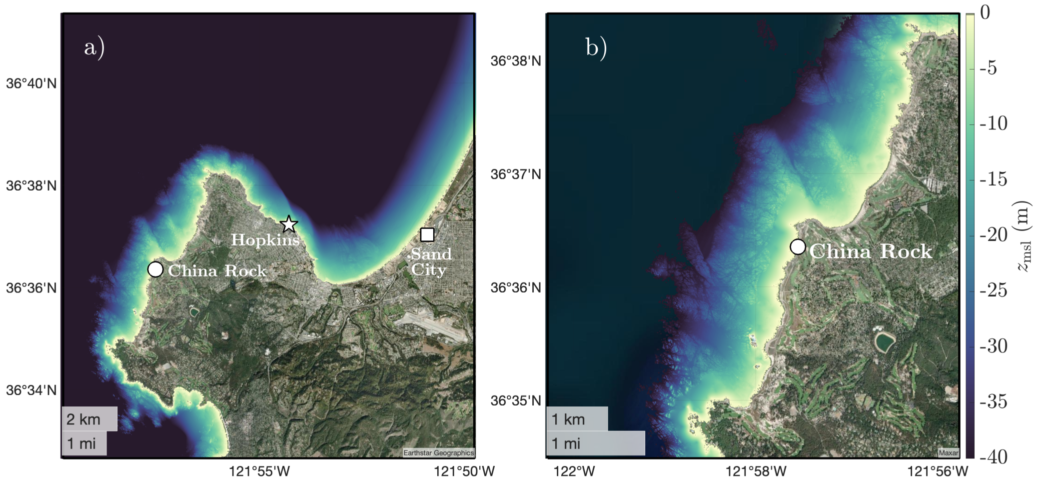

Figure 1. Bathymetric maps of: a) the Monterey Peninsula, CA, USA, and b) the western edge of the peninsula near China Rock. Color shading indicates negative bathymetric elevation relative to mean sea level (z_{msl}) in meters with the colorbar provided on the right. Notable geographic locations for China Rock, Hopkins Marine Station, and Sand City are annotated for reference.

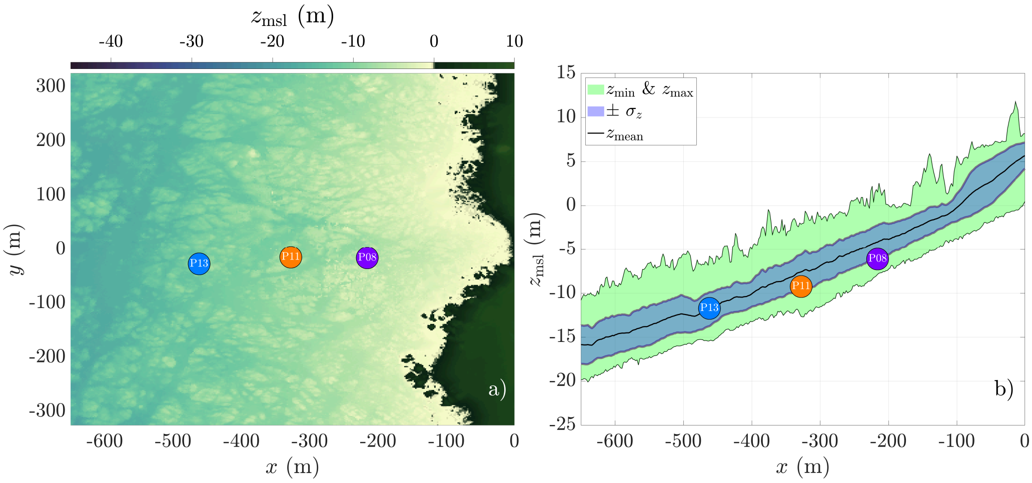

Figure 2. a) Bathymetric map of China Rock, Pebble Beach, CA, USA, situated on the outer edge of the Monterey Peninsula as a function of a local cross-shore x and alongshore y coordinate system. A colorbar at the top indicates elevations relative to mean sea level z_{msl}. Instrument stations with their corresponding numbers representing their mean depths are overlaid on top. b) An alongshore-averaged profile z_{mean} displays alongshore standard deviations $\pm\sigma_z$, alongshore maxima z_{max}, and alongshore minima z_{min} as a function of the cross-shore x.

by scientific divers, covering water depths ranging from 8 to 13 m. The station names correspond to the field site (i.e., P for pressure sensors) and their average water depths, h, as indicated by the subsequent numbers (P13, P11, and P08), as shown in Figure 2. The instrument locations are also provided in the local coordinate system, where the stations were located in the cross-shore at $x = -462, -327$, and -216 m. Analysis of instrument pairs will be represented as (PXX, PYY). The pressure sensors were arranged in a cross-array to assess the cross-shore evolution of SS and IG waves. The emphasis here is on IG waves deeper than 8 m, ensuring that the measurements are: 1) located on the inner shelf, outside the surf zone and 2) offshore from the heterogeneous shoreline variability of the headlands and embayments (e.g., Winter et al., 2017; Quinn et al., 2025) and the fine-scale rocky variability associated with surge channels (e.g., MacMahan et al., 2023).

2.2 Analysis

Sea-swell (SS, within the 0.04−0.2 Hz frequency band) and infragravity waves (IG, within the 0.005−0.04 Hz frequency band) are analyzed via sea surface elevation spectra $G_{\eta\eta}(f)$ derived from pressure data using linear wave theory (e.g., Guza & Thornton, 1980; Marques et al., 2024). The stations are located at depths shallower than 15 m, which is the maximum depth for categorizing the IG frequency band as shallow water. Here, the wavenumber k for $f = 0.04$ Hz, the upper frequency limit for IG band, multiplied by $h = 15$ m, is less than $\frac{\pi}{10}$. Auto-spectra, cross-spectra, and bispectra are computed two-hourly (every two hours) with 10-minute Hamming windows that have a 50% overlap, resulting in 64 degrees of freedom, similar to the IG spectral analysis conducted by Ruessink (1998) and Thomson et al. (2006). The SS E_{SS} and IG E_{IG} surface elevation variances (m^2) are proportional to wave energy defined as

$$E_{\mathrm{SS,IG}} = \int_{\mathrm{SS,IG}} G_{\eta\eta}(f)df, \tag{1}$$

obtained by integrating the sea surface energy density spectrum $G_{\eta\eta}(f)$ across their respective SS and IG frequency f bands, denoted by the corresponding subscripts of SS and IG, and henceforth simply referred to as energies. The significant wave height in the SS band, represented as H_{SS}, and in the IG band, expressed as H_{IG}, are calculated as

$$H_{\mathrm{SS,IG}} = 4\sqrt{E_{\mathrm{SS,IG}}}. \tag{2}$$

The spectrally-weighted mean wave periods for sea-wavesT_{SS} and IG waves T_{IG} are computed by integrating the spectrum across their respective SS and IG frequency f bands,

$$T_{\mathrm{SS,IG}} = \frac{\int_{\mathrm{SS,IG}} G_{\eta\eta}(f)df}{\int_{\mathrm{SS,IG}} f \cdot G_{\eta\eta}(f)df}. \tag{3}$$

Cross-spectral analysis is performed between instrument pairs and denoted as $G_{\Delta x}$. It is used to characterize the frequency structure of IG waves, distinguishing between standing (e.g., Suhayda, 1974; Sheremet et al., 2002) and progressive wave behavior (e.g., de Bakker et al., 2014; Pomeroy et al., 2012). The analysis also provides estimates of cross-shore propagation.

The nonlinear triad interaction transfer N_{IG} (e.g., Herbers & Burton, 1997; Henderson & Bowen, 2002; Thomson et al., 2006) and bicoherence $|b_{\mathrm{i}}(\Delta f)^2|$ including biphase $\overline{\alpha}_{\mathrm{bi}}$ (e.g., Herbers et al., 1994) are calculated from the bispectrum $B(f, \Delta f)$, defined as

$$B(f, \Delta f) = \mathbb{E}[X(f)X(\Delta f)X(f + \Delta f)] \tag{4}$$

where $\mathbb{E}$ is the expected value and $X(f)$ is the complex Fourier amplitudes of the sea surface elevation. The rates of nonlinear energy transfer N_{IG} between the IG waves and the higher-frequency waves are estimated as (e.g., Herbers & Burton, 1997):

$$N_{\mathrm{IG}} = \int_{IG} 3\pi f h \int_{-\mathrm{SS}}^{\mathrm{SS}} \Im\left[B(f', f - f')\right] df'\, df \tag{5}$$

where B is the bispectrum (Eq. 4) constructed from the sea surface elevation (e.g., Kim & Powers, 1979; Elgar & Guza, 1985), which is integrated over the imaginary contribution of the frequency pairs $(f', f-f')$ to analyze the difference interaction between the IG frequency f and the short-wave frequency f'. The code was provided by Martins (2024) as applied in Martins, Bonneton, Lannes, and Michallet (2021); Martins, Bonneton, and Michallet (2021); Martins et al. (2023); Sous et al. (2023).

3 Results

3.1 Summary of Sea Swell & Infragravity Waves

The SS significant wave heights H_{SS} are consistent across P13, P11, and P08 (Figure 3a), displaying a slight decrease from P13 to P08, which corresponds with bottom friction dissipation attributed to the rough rocky seabed (Gon et al., 2020; Marques, Feddersen, MacMahan, Acevedo-Ramirez, & Suanda, 2025). From June to mid-September, H_{SS} fluctuates between approximately 0.75 and 2 m, influenced by smaller synoptic storms and diurnal wind effects. After mid-September, larger synoptic storms drive H_{SS} to reach heights of up to 4 m with subsiding diurnal H_{SS} variability. Conversely, the IG significant wave height H_{IG} is lowest offshore and increases as depth decreases, though correlated with H_{SS} over time (Figure 3b), consistent with most field observations along sandy shores (e.g. Elgar et al., 1992) and coral reefs (e.g., Pomeroy et al., 2012). The H_{IG} remains relatively low around 0.05 m from June to mid-September but experiences a substantial increase thereafter, reaching up to 0.6 m. The mean wave period of the sea swell T_{SS} is comparable for P13, P11, and P08 (Figure 3c). From June to mid-August, T_{SS} hovers around 7 s due to increased local SS wave generation. After this period, it rises with the arrival of synoptic winter storms, generated much farther away. Similarly, the IG mean wave period T_{IG} is comparable for P13, P11, and P08 (Figure 3d). The T_{IG} maintains a relatively constant value at 46 s, with slight variation during the largest storm event in October. The reason for the relatively constant T_{IG} is explained in Section 3.2 when examining the sea surface elevation spectra in detail. The observed SS waves (Figure 3a,c) correspond with the summer and fall conditions, consistent with those described for the Monterey region (e.g., Xu, 1999; Hendrickson & MacMahan, 2009; Hlywiak et al., 2023; Benbow & MacMahan, 2024; Collins et al., 2024). The tides display a mixed semidiurnal pattern (Figure 3e), characteristic of the central California coastline (e.g., Nidzieko, 2010).

3.2 Infragravity Spectral Relationships

The IG spectral response is analyzed to assess how spectral energy varies with frequency and time, helping to identify appropriate IG limits, potential contamination from other processes, and the presence of nodal structures associated with standing waves. The analysis is comparable to Herbers, Elgar, Guza, and O'Reilly (1995), which characterized the IG spectral shapes at various US coastal sites and Hawaii for depths greater than or equal to 8 m. They found that the frequency limits of the IG band and the cross-shore variation exhibit a spectral shape with nodal structure close to shore, and more consistent estimates farther offshore. The two-hourly sea surface elevation spectra $G_{\eta\eta}(f)$ were normalized by the two-hourly IG-band variance,

$$G_{\mathrm{norm}}(f) = \frac{G_{\eta\eta}(f)}{E_{\mathrm{IG}}}. \tag{6}$$

These normalized spectra $G_{\mathrm{norm}}(f)$ are depicted in Figure 4a–c along with the time-averaged $\overline{G}_{\mathrm{norm}}(f)$ for the entire experiment (Figure 4d). Throughout the experiment, $G_{\mathrm{norm}}(f)$

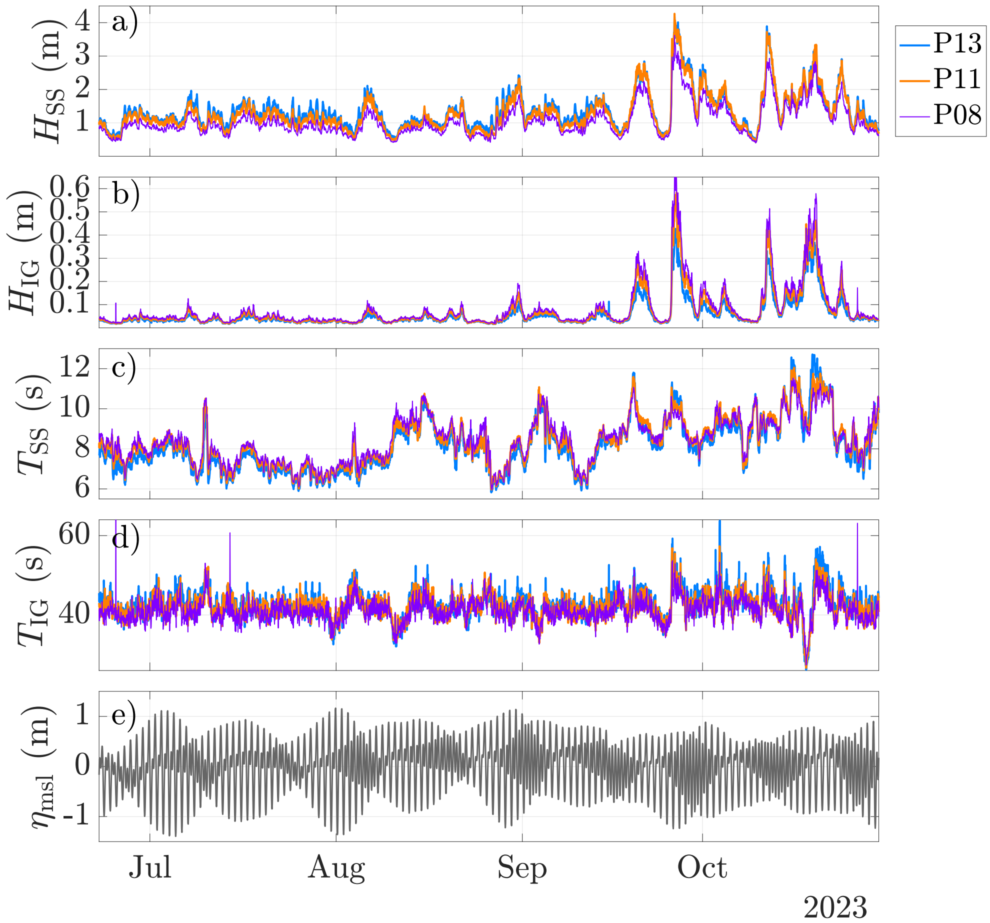

Figure 3. The experimental time series is shown for a) SS significant wave height H_{SS}, b) IG significant wave height H_{IG}, c) SS mean wave period, T_{SS}, d) IG mean wave period T_{IG} for P13 (blue), P11 (orange), and P08 (purple), and e) mean sea level η_{msl}. The station locations are provided in Figure 2.

across the cross-shore array remains mostly constant with frequency for the IG band, $0.005 \leq f \leq 0.04$ Hz (gray lines, Figure 4a–c), consistent across stations. The spectral flatness remains unaffected by storm events or tidal modulations (Figure 3).

The time-averaged spectra $\overline{G}_{\mathrm{norm}}(f)$ show the general response (Figure 4d). Beyond $f \geq 0.04$ Hz, energy increases due to SS contributions, defining the upper-frequency limit of the IG band. A slight decrease in energy occurs for $0.005 \leq f \leq 0.01$ Hz, with strong frequency nodal structures for $f \leq 0.005$ Hz, likely from continental shelf motions (e.g., Herbers, Elgar, Guza, & O'Reilly, 1995) that persist until $f \leq 0.01$ Hz. The flatness of the IG spectral energy explains why the mean IG wave periods T_{IG} remain relatively constant (Figure 3d), occurring near the mid-point of the IG frequency band ($f = 0.005$ Hz and $f = 0.04$ Hz). For P13, P11, and P08, the absence of frequency nodes and antinodes, which are common on sandy beaches (e.g. Suhayda, 1974; Herbers, Elgar, Guza, & O'Reilly, 1995), suggests minimal influence of standing waves.

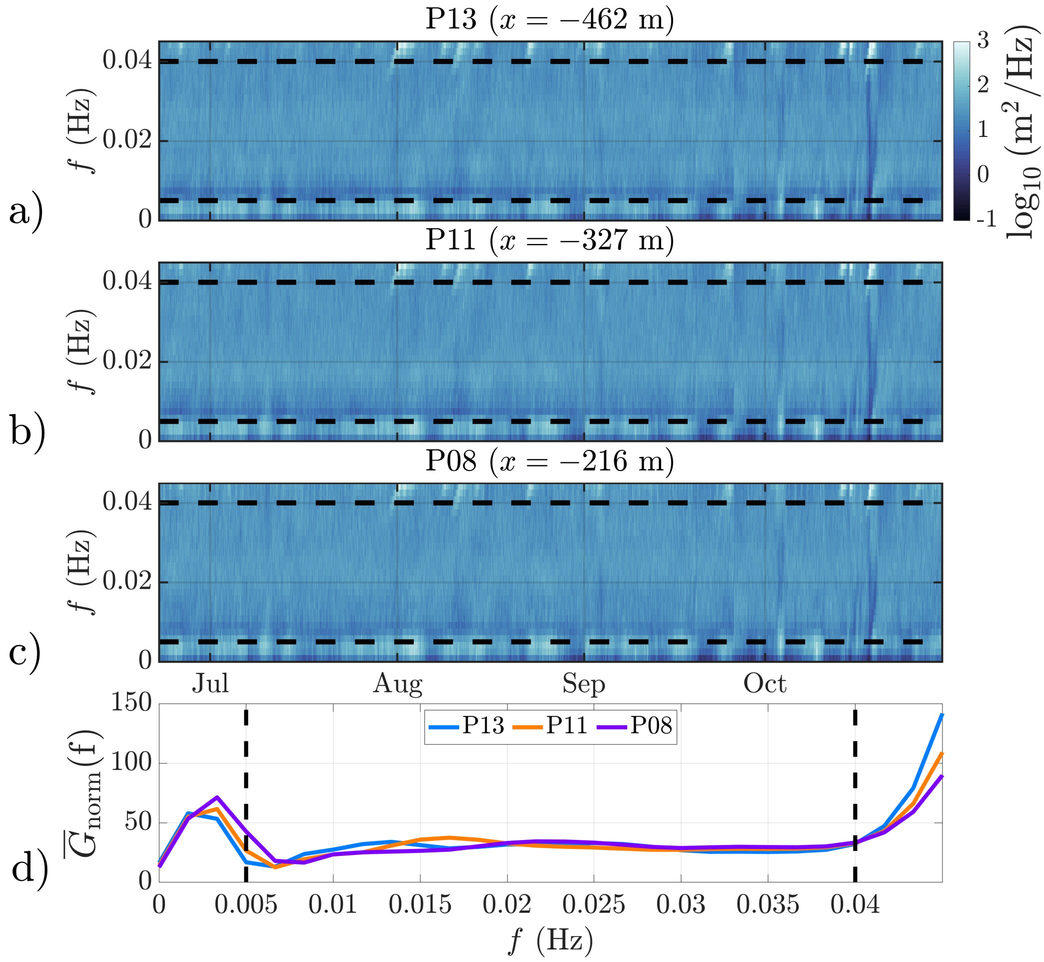

Figure 4. a-c) Timestacks of two-hourly sea surface elevation spectra $G_{\mathrm{norm}}(f)$ (Equation 6) are contoured in $\log_{10}$-scale as a function of time and frequency for P13, P11, and P08; see Figure 2 for their locations. The cross-shore location relative to the shoreline x is indicated in the title. The colorscale is plotted to the far right. d) The time-averaged normalized IG spectra $\overline{G}_{\mathrm{norm}}(f)$ for the four stations are plotted as a function of frequency. The overlaid horizontal black lines on a–c) and vertical black lines on d) represent the frequency limits for the IG band, $0.005 \le f \le 0.04$ Hz.

At all three stations, the IG spectral energy per frequency over time $G_{\eta\eta}(f,t)$ is correlated with the offshore integrated SS energy $E_{SS,P13}(t)$ at station P13 (Figure 5). Similar to Herbers, Elgar, Guza, and O'Reilly (1995), the correlation coefficient $r(f)$ generally remains above 0.6 for IG frequencies, indicating that spectral variations are associated with the integrated SS energy, which suggests local forcing. The correlation significance for 95% is $r(f) > 0.24$. The correlation coefficient diminishes for $f < 0.005$ Hz and $f \ge 0.04$ Hz, suggesting these as suitable frequency limits for investigating IG motions on rocky shores.

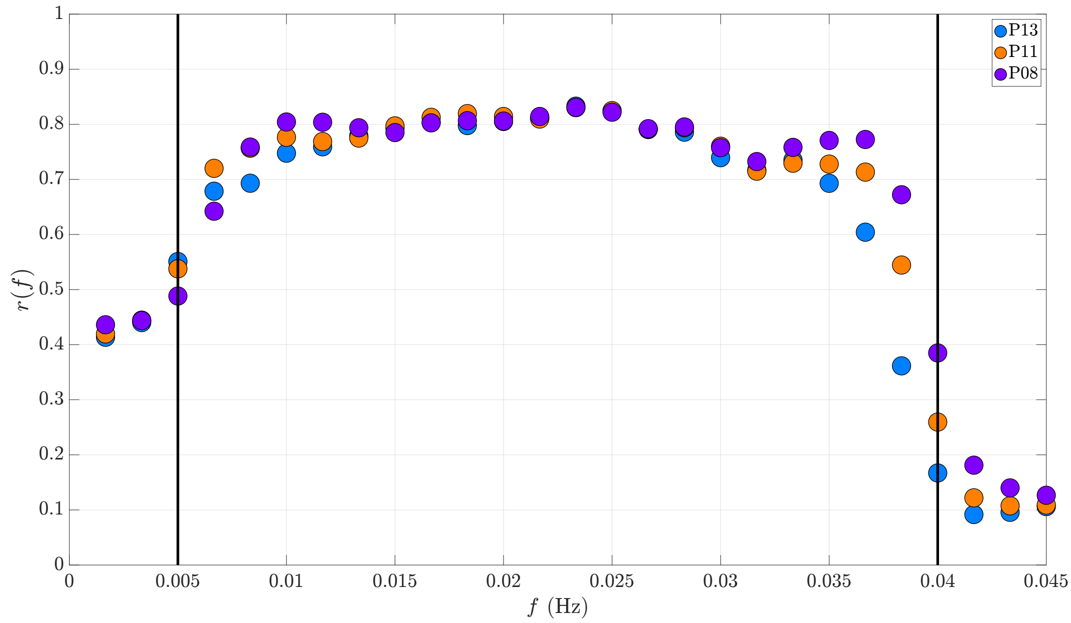

Figure 5. The cross-correlation coefficient $r(f)$ between $G_{\eta\eta}(f,t)$ and $E_{SS,P13}(t)$ versus frequency f. The dots indicate the correlation coefficients, with varying colors representing stations P13, P11, and P08. The correlations are significant with 95% confidence for $r(f) > 0.244$. Vertical black lines mark the frequency limits for the IG band, $0.005 \leq f \leq 0.04$ Hz.

3.3 Infragravity Phase Difference Spectra

Cross-spectral analysis was performed to characterize the spectral phase difference, which reveals the cross-shore structure and propagation of IG waves. Stations P11 and P08 are examined with the offshore station P13. The spectral phase difference, denoted as $\Delta\alpha(f)$, was calculated using

$$\Delta\alpha(f) = \tan^{-1}\left(\frac{\Im[G_{\Delta \mathrm{x}}(f)]}{\Re[G_{\Delta \mathrm{x}}(f)]}\right), \tag{7}$$

where $\Re[G_{\Delta \mathrm{x}}(f)]$ and $\Im[G_{\Delta \mathrm{x}}(f)]$ represent the real and imaginary components of the two-hourly cross-spectrum $G_{\Delta \mathrm{x}}(f)$ and Δx represents cross-shore separation distance. The instrument time differences are minimal (see Appendix A). For station pairs (P13, P11) and (P13, P08), the two-hourly $\Delta\alpha(f)$ is contoured as a function of time and frequency, with frequencies extending to $f = 0.09$ Hz, representing the lower band of SS waves, which helps in visualizing the $\Delta\alpha(f)$ structure (Figure 6a,b). The $\Delta\alpha(f)$ estimates exhibit a sawtooth pattern indicative of progressive wave behavior observed for IG and SS waves. The color representation of $\Delta\alpha(f)$ increases linearly until $\Delta\alpha = 180°$ is reached, then abruptly transitions to $\Delta\alpha = -180°$ owing to phase wrapping, subsequently linearly increasing again, and repeating when $\Delta\alpha = 180°$. The sawtooth pattern is more easily understood by time-averaging $\overline{\Delta\alpha}(f)$ over the first 30 days (Figure 7), during which the sensor clock drifts are considered small (see Appendix A).

The sawtooth pattern arises from the circular nature of $\Delta\alpha(f)$ being defined between $-180°$ and $180°$. For a progressive wave, $\Delta\alpha(f)$ can be described as

$$\Delta\alpha(f) = \frac{\Delta x}{\langle C(f,h)\rangle} 2\pi f, \tag{8}$$

where Δx is the distance between stations and $\langle C(f,h)\rangle$ is the spatially-averaged phase speed as a function of frequency f and water depth h. For the IG band in shallow water at depths less than 15 m, the phase speed is nondispersive and is therefore represented as $\langle C(h)\rangle$, as a function of water depth. For a constant $\langle C(h)\rangle$, $\Delta\alpha(f)$ linearly increases with f. As Δx increases, the slope of $\Delta\alpha(f)$ is steeper, resulting in more $\Delta\alpha(f)$ transitions at $\Delta\alpha = \pm 180°$ (Figures 6a,b, 7). The sawtooth pattern of $\Delta\alpha(f)$ is evident across both station pairs, and the behavior is consistent from the IG band into the SS band, consistent with a progressive wave (see Figures 6a,b, 7). Small variations in $\Delta\alpha(f)$ are observed, likely due to variations in $\langle C(h)\rangle$ associated with tidal changes in water depth, altering $\Delta\alpha(f)$ in Equation 8. In addition, variable incoming wave directions will cause slight temporal variations in $\Delta\alpha(f)$. Generally, a consistent sawtooth pattern emerges, indicating predominantly progressive IG waves propagating shoreward, suggesting most of its energy is dissipated shoreward of P08. The sawtooth pattern is consistent with IG observations in shallower water across a coral reef flat (Pomeroy et al., 2012). If standing waves were present, the $\Delta\alpha(f)$ would support a square wave pattern (e.g., Suhayda, 1974), which is not observed here.

For comparison, a theoretical $\Delta\alpha(f)$ is computed using the identical instrument pairs, where $C(h)$ is estimated at each station location using linear wave theory and then spatially-averaged, denoted as $\langle\cdot\rangle$, shown in Figure 6b,f. Good agreement is observed between the theoretical $\Delta\alpha(f)$ and the observational $\Delta\alpha(f)$, suggesting a shoreward progressive "free" wave that propagates according to a linear dispersion relationship. Likewise, the similarity is more easily seen by time-averaging $\Delta\alpha(f)$ for the first 30 days, shown in Figure 7. In addition, $\Delta\alpha(f)$ for $C(f,h)$ (a function of frequency and water depth) is computed for a bound IG wave that would propagate at the wave group speed (Figure 6e,f, 7) at the mean period of SS waves (Figure 3c). There are more temporal variations in the bound wave phase due to changes in the SS wave period T_{SS}. However, although sawtooth in nature, the patterns do not align with observations. In summary, the phase difference spectra indicate that the IG waves are primarily shoreward progressive and follow a linear wave dispersion relationship, suggesting that they are free waves.

Most parameterizations of IG dissipation and reflection for sandy shores, such as in Battjes et al. (2004) with laboratory data, define a normalized bed slope parameter β_z,

$$\beta_z = \frac{h_x}{\omega}\sqrt{\frac{g}{H_{\mathrm{IG}}}}, \tag{9}$$

where h_x is the bottom slope and ω is the radian IG frequency. The parameter β_z does not apply to the rocky shore observations at China Rock. For example, when $\beta_z < 1.25$, Van Dongeren et al. (2007) suggested that IG waves represent a mild-sloping regime, where

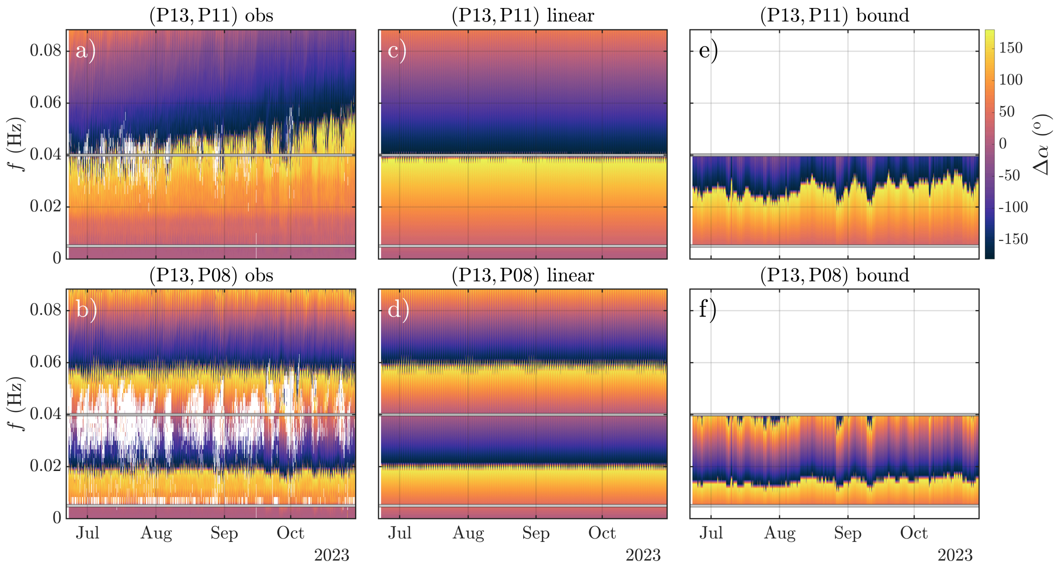

Figure 6. Timestacks of two-hourly phase difference spectra $\Delta\alpha(f)$ relative to P13 are contoured as a function of time and frequency for a) P11 and b) P08. The cross-shore separation distance Δx relative to P13 is 135 and 246 m. The white regions indicate coherence values that fall below the 95% significance level. The overlaid gray lines represent the frequency limits for the IG band, $0.005 \leq f \leq 0.04$ Hz. The $\Delta\alpha(f)$ colorscale is plotted to the far upper right. c, d) For each corresponding pair of stations, a theoretical $\Delta\alpha(f)$ are contoured as a function of time and frequency based on a linear phase speed. e, f) For each corresponding pair of stations, a theoretical $\Delta\alpha(f)$ are contoured as a function of time and frequency based on a bound wave group phase speed.

the IG energy is primarily dissipated by wave breaking. For $\beta_z > 1$ on steep slopes, like those found here, a large IG reflection regime would occur, corroborated by modeling efforts (Ruju et al., 2012). Field experiments by de Bakker et al. (2014) and Inch et al. (2017) suggested that the transition likely occurs at a higher β_z, around 3. de Bakker et al. (2014) found that lower frequencies of IG waves could be standing due to shoreline wave reflections, while at higher IG frequencies, they were progressive due to shoreline dissipation. Here, $\beta_z \approx 2.5$, implying IG reflections would be significant, yet the frequency nodal structure (Figure 4) and phase propagation disagree (Figure 6). The progressive wave pattern found here contrasts with many sandy beach observations that found standing wave patterns (e.g., Suhayda, 1974; Huntley, 1976; Sheremet et al., 2002; MacMahan et al., 2004), although it is consistent with some observations at higher IG frequencies (e.g., de Bakker et al., 2014).

3.4 Infragravity Energy Comparisons

The two-hourly IG energy at station P13, $E_{\mathrm{IG,P13}}$, is compared to the two-hourly IG energy, E_{IG}, at the shoreward stations P11 and P08. A linear regression is applied assuming a zero intercept ($b = 0$). The resulting linear slopes m increase from 1.67 to

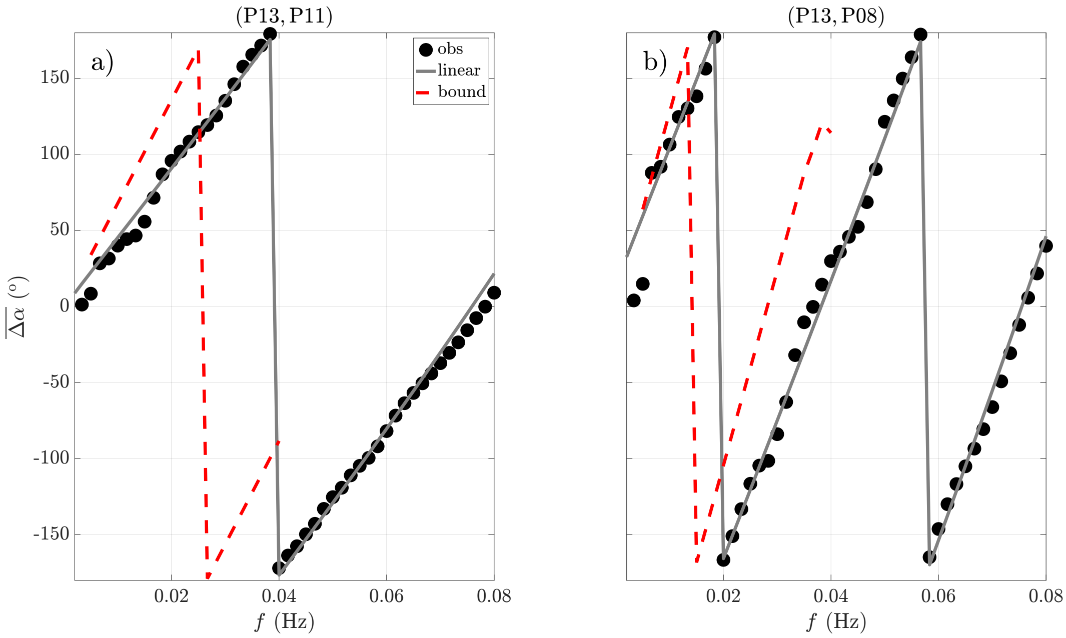

Figure 7. First 30-day time average for $\Delta\alpha(f)$ as a function of frequency f for a) (P13,P11) and b) (P13,P08) for the observations (black dots), a linear phase speed estimate (gray line), and bound wave group speed estimate (red dashed line), as shown in Figure 6.

2.3, while R^2 values remain near one but decrease slightly with decreasing depth and increasing distance from P13 (Figure 8; slope m and R^2 are reported in the subplot titles). The decrease in R^2 suggests decorrelation of IG wave energy as it propagates shoreward and interacts with the rough, rocky bottom. Nevertheless, a strong linear relationship persists between offshore and shallower IG energy.

The IG amplification can be modeled as $E_{\mathrm{IG},2}/E_{\mathrm{IG},1} = (h_1/h_2)^{-n}$, where $n = 0.5$ indicates that IG energy is conserved following Green's Law, where increases of energy are associated with shoaling (e.g., Elgar et al., 1992). The IG energy found above the Green's Law prediction, i.e., greater than $(h_1/h_2)^{-0.5}$, implies an influx of energy (Elgar et al., 1992), potentially from mechanisms such as edge wave resonance (e.g., Herbers, Elgar, & Guza, 1995), bound wave generation (e.g., Longuet-Higgins & Stewart, 1962), and nonlinear triad interactions (e.g., Herbers & Burton, 1997; Norheim et al., 1998; Henderson et al., 2006; Thomson et al., 2006). Conversely, energy below $(h_1/h_2)^{-0.5}$ suggests an outflux of energy, typically due to dissipation by bottom friction (e.g., Henderson & Bowen, 2002; Pomeroy et al., 2012), seaward of wave breaking. Observations on sandy beaches generally show IG energy consistent with, or exceeding, Green's Law (e.g., Thomson et al., 2006; Sheremet et al., 2002; Ruessink, 1998), indicating a combination of contributing processes. In this study, IG amplification varies both with E_{IG} and among station pairs (Figure 8). While this variability is broadly consistent with previous sandy shore observations (e.g., Elgar et al., 1992; Herbers, Elgar, & Guza, 1995; Thomson et al., 2006), the observed range here is notably larger. For the station pair

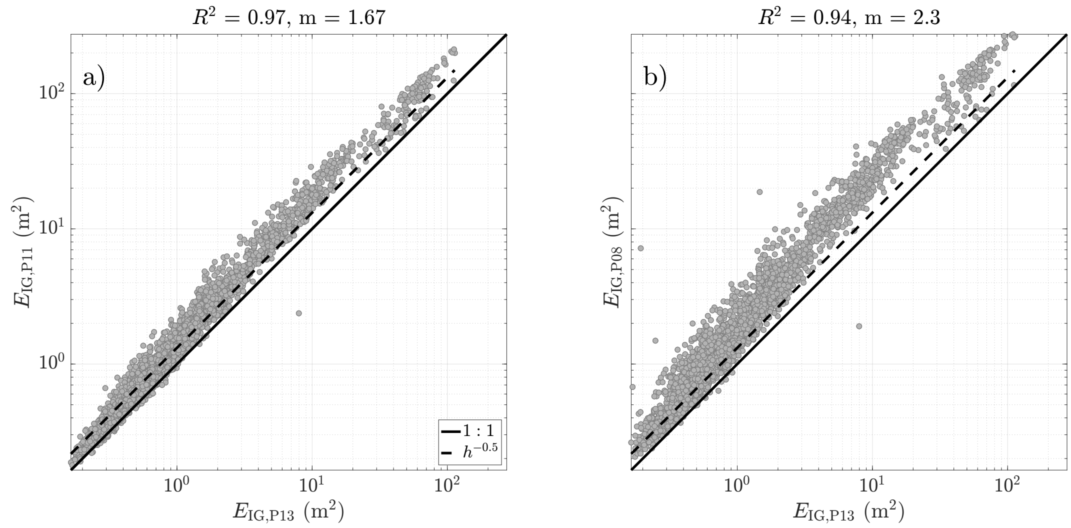

Figure 8. The IG energy E_{IG} at a) P11 and b) P08 is plotted as a function of IG energy at P13 $E_{IG,P13}$ (top row). The title above each subplot provides the linear fit statistics. The lines represent the fits for $1:1$ and $h^{-0.5}$.

(P13, P11) (Figure 8a), amplification follows $(h_1/h_2)^{-0.5}$ for low energy levels ($E_{\mathrm{IG}} < 10^0$ m^2), exceeds Green's Law at intermediate energy levels (10^0 m^2 $< E_{\mathrm{IG}} < 10^1$ m^2), and significantly exceeds it at high energy levels ($E_{\mathrm{IG}} > 10^1$ m^2). For the pair (P13, P08) (Figure 8b), amplification consistently exceeds $(h_1/h_2)^{-0.5}$ across most energy levels. No consistent amplification pattern emerges across the whole energy range and among different station pairs, indicating that a complete interpretation requires an energy balance that includes nonlinear energy transfers (e.g., Thomson et al., 2006) and bottom frictional dissipation (e.g., Pomeroy et al., 2012), as discussed in Section 4.1.

3.5 Bound & Free Infragravity Contributions

The bispectral analysis estimates the relative fraction of bound IG energy (e.g., Herbers et al., 1994; Ruessink, 1998). The bicoherence for the IG band, referred to as $|b_{\mathrm{i}}(\Delta f)|^2$, is estimated by integrating the normalized bispectrum $B(f, \Delta f)$, (Eq. 4), constructed from the sea surface elevation for Δf to 0.2 Hz frequencies, following Haubrich (1965), as defined:

$$|b_{\mathrm{i}}(\Delta f)|^2 = \frac{2\int_{\Delta f}^{0.2\ \mathrm{Hz}} |B(f,\Delta f)|^2 df}{\int_{\Delta f}^{0.2\ \mathrm{Hz}} \mathbb{E}[|X(f)|^2]\mathbb{E}[|X(\Delta f)|^2]\mathbb{E}[|X(f+\Delta f)|^2]}, \tag{10}$$

where $\mathbb{E}$ is the expected value and $X(f)$ is the complex Fourier amplitudes of the sea surface elevation (see Herbers et al., 1994). The fraction of bound IG energy $E_{\mathrm{IG,BND}}$ to the total IG energy E_{IG} is given by:

$$\frac{E_{\mathrm{IG,BND}}}{E_{\mathrm{IG}}} = \frac{\int_{0.005}^{0.04\ \mathrm{Hz}} |b_{\mathrm{i}}(\Delta f)|^2 G_{\eta\eta}(f)df}{\int_{0.005}^{0.04\ \mathrm{Hz}} G_{\eta\eta}(f)df}. \tag{11}$$

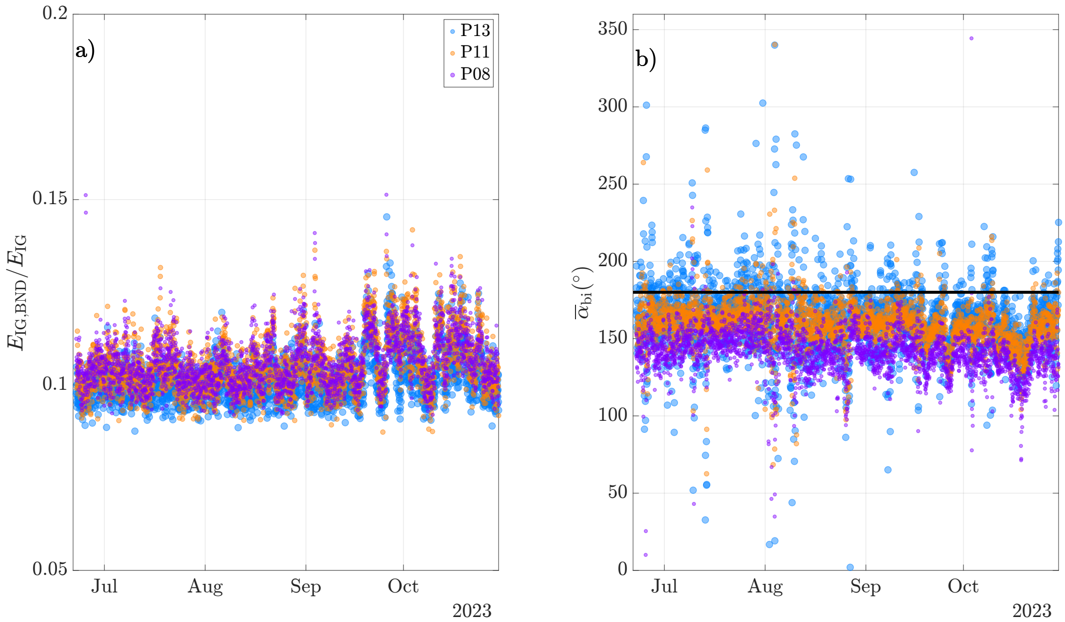

Figure 9. The experimental time series is shown for a) the relative bound-to-total IG energy $E_{\mathrm{IG,BND}}/E_{\mathrm{IG}}$ (Equation 11), and b) the biphase α_{bi} associated with the bound wave contribution for P13 (blue), P11 (orange), and P08 (purple). The black line represents $\alpha_{bi} = 180^\circ$. The instrument locations are provided in Figure 2.

The relative bound-to-total IG energy $E_{\mathrm{IG,BND}}/E_{\mathrm{IG}}$ is constant at around 0.1 (Figure 9a) for P13, P11, and P08 with small variations related to increased storm activity (Figure 3a). The bound wave energy for these rocky shores is smaller than $E_{\mathrm{IG,BND}}/E_{\mathrm{IG}} = 0.3$ for southern California sandy beaches in depths of 10-15 m (Lange et al., 2024). For sandy shores, relative bound-to-total IG energy $E_{\mathrm{IG,BND}}/E_{\mathrm{IG}}$ decreases to near zero within the surf zone (e.g., Ruessink, 1998; Sheremet et al., 2002). The finding that over 90% of the IG energy is free on these rocky shores provides compelling evidence that its propagation adheres to linear dispersion, reinforcing the interpretation outlined in Section 3.3.

The average biphase $\overline{\alpha}_{\mathrm{bi}}$ for the bound wave contribution is estimated as

$$\overline{\alpha}_{\mathrm{bi}} = \tan^{-1}\left(\frac{\overline{\Im(B(f,\Delta f))}}{\overline{\Re(B(f,\Delta f))}}\right), \tag{12}$$

where $\Re$ and $\Im$ are the real and imaginary components, and the overline denotes the two-dimensional average of the bispectrum for the IG frequency bands (e.g., de Bakker, Tissier, & Ruessink, 2016). Note the $\alpha_{\mathrm{bi}}(f)$ estimates are stable for high bicoherence but tend to be randomly distributed for low bicoherence, with stability improving as the number of degrees of freedom increases (Elgar & Guza, 1985), here further increased due to averaging in Eq. 12. Overall, $\overline{\alpha}_{\mathrm{bi}}$ is generally stable, though some noise remains (Figure 9b). For P13, the bound IG wave has a biphase $\overline{\alpha}_{\mathrm{bi}}$ of approximately 180° that decreases slightly for P11 and continues decreasing for P08 (Figure 9b), consistent with nonlinear transfer from the SS to the IG waves (e.g., Janssen et al., 2003), and consistent with sandy beach biphase estimates (e.g., Elgar & Guza, 1985; Ruessink, 1998; Lange et al., 2024).

4 Discussion

4.1 Cross-shore Wave Energy Flux Balance

The analysis in Section 3.3 indicates that IG waves are progressive waves, and that all the energy variance E_{IG} is considered to propagate shoreward. Rates of energy dissipation and nonlinear transfer within the IG band are quantified using the cross-shore wave energy flux balance equation (e.g., Henderson & Bowen, 2002; Henderson et al., 2006; Thomson et al., 2006; Pomeroy et al., 2012):

$$\frac{\partial F_{\mathrm{IG}}^{+}}{\partial x} = N_{\mathrm{IG}} + D_{\mathrm{IG}}, \tag{13}$$

where F_{IG}^{+} represents the shoreward variance flux, N_{IG} describes nonlinear transfer of energy at IG frequencies due to SS wave-wave (triad) interactions (Herbers & Burton, 1997), and D_{IG} indicates the dissipation of IG wave energy through bottom friction.

The IG energy (variance) flux gradient $\partial F_{\mathrm{IG}}^{+}/\partial x$ and nonlinear energy transfer N_{IG} for station pairs (P13, P11) and (P11, P08) are plotted as a function of time from September 18 to October 28, when SS and IG signals are the largest (Figure 10a,b). The $\partial F_{\mathrm{IG}}^{+}/\partial x$ and N_{IG} support a strong temporal correlation, $r = 0.96$ for (P13, P11) and $r = 0.89$ for (P11, P08). For (P13, P11), which are deeper, the magnitudes are similar, though there are times when N_{IG} is greater than $\partial F_{\mathrm{IG}}^{+}/\partial x$ (Figure 10c). For (P11, P08), which are shallower, the magnitudes are similar, though N_{IG} tends to be greater than $\partial F_{\mathrm{IG}}^{+}/\partial x$ more frequently (Figure 10d). These results suggest that nonlinear transfer through triad interactions is responsible for the onshore increase in IG wave energy, analogous to Thomson et al. (2006) and Henderson et al. (2006), which observed similar behavior on the inner shelf of a sandy beach. The observation that N_{IG} estimates tend to be larger than $\partial F_{\mathrm{IG}}^{+}/\partial x$ estimates suggests that the excess N_{IG} is likely balanced by bottom dissipation (e.g., Henderson & Bowen, 2002; Henderson et al., 2006; Pomeroy et al., 2012), in particular owing to the increased bottom roughness by the rocky seabed relative to sandy shores (e.g., Gon et al., 2020; Marques, Feddersen, MacMahan, Acevedo-Ramirez, & Suanda, 2025). The importance of bottom friction is explored in greater detail in the following section. Note that the N_{IG} energy transferred relative to the cross-shore SS energy flux ($\partial F_{\mathrm{SS}}^{+}/\partial x$) on average is less than 0.004. Thus, the nonlinear energy transfer is considered minor for computations of SS bottom dissipation estimates (e.g., Sous et al., 2023; Marques, Feddersen, MacMahan, Acevedo-Ramirez, & Suanda, 2025), consistent with SS and IG observations on sandy shores (e.g., Henderson et al., 2006). It is also consistent with weak nonlinear transfer owing to steep bottom slopes (e.g., Herbers & Burton, 1997; Norheim et al., 1998; de Bakker, Tissier, & Ruessink, 2016).

Recent alternative theories, such as those in Contardo et al. (2021), suggest that bathymetric steps—like those associated with coral reefs can convert IG bound waves

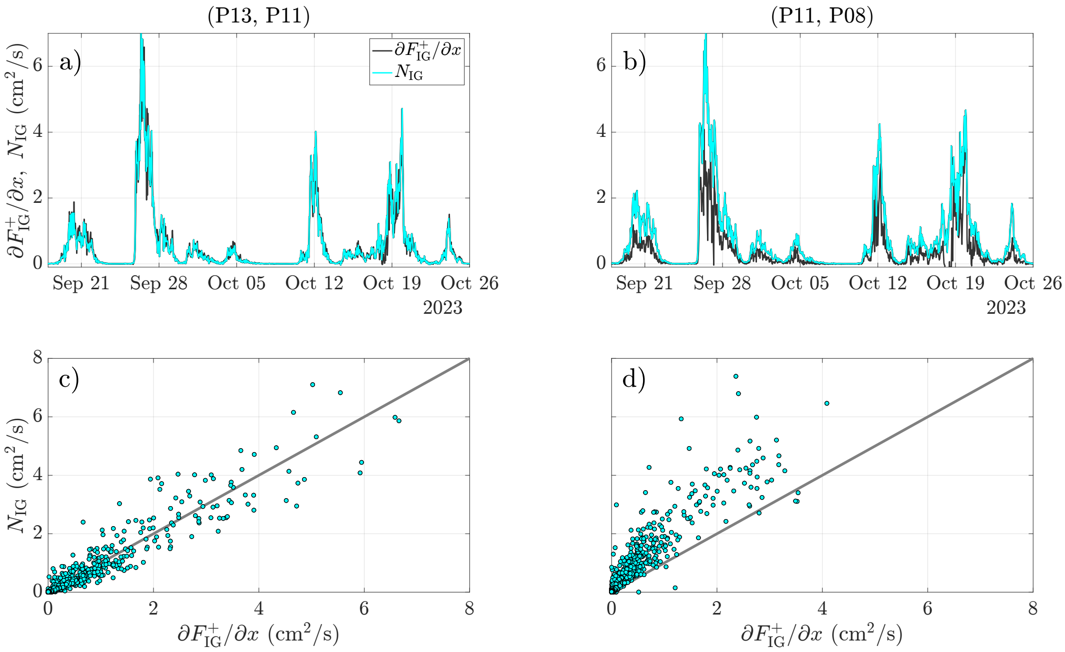

Figure 10. (top) IG variance flux gradient $\partial F^+_{\mathrm{IG}}/\partial x$ (black line) and nonlinear energy transfer N_{IG} (cyan line) for station pairs a) (P13, P11) and b) (P11, P08) versus time from September 18 to October 28. (bottom) The nonlinear energy transfer N_{IG} versus $\partial F^+_{\mathrm{IG}}/\partial x$ for the entire measurement record for station pairs c) (P13, P11) and d) (P11, P08). The black line represents the 1:1 relationship.

into free waves without requiring SS wave breaking. They further extended this mechanism to a continuous profile representing a series of steps for steep profiles, where bound and free IG waves continue to evolve and subsequently release both shoreward- and seaward-propagating free IG waves. Based on our analysis, which is consistent across various approaches, a simple shoreward-propagating free wave forced by nonlinear triads appears to be the most suitable mechanism, contrary to this alternative.

4.2 Bottom Frictional Dissipation & Friction Factors

Infragravity wave energy dissipation by bottom friction can be parameterized by a friction factor f_e through

$$D_{\mathrm{IG}} = f_e \frac{0.8}{g} U_{\mathrm{SS}} U_{\mathrm{IG}}^2, \tag{14}$$

where U represents the root-mean-square orbital velocity amplitude at the bottom (e.g., Henderson & Bowen, 2002; Henderson et al., 2006; Van Dongeren et al., 2007; Pomeroy et al., 2012). Following the approach of Marques, Feddersen, MacMahan, Acevedo-Ramirez, and Suanda (2025) for SS waves, the bottom dissipation for IG waves is expressed as:

$$D_{\mathrm{IG}} = f_e \frac{0.8}{g} \langle U_{\mathrm{SS}} \rangle \langle U_{\mathrm{IG}} \rangle^2, \tag{15}$$

where $\langle U \rangle$ is spatially-averaged between corresponding instrument pairs denoted with an $\langle \cdot \rangle$. The U_{SS} at the bottom is computed using linear wave theory,

$$U_{\mathrm{SS}} = \frac{H_{\mathrm{SS,rms}}}{2} \frac{2\pi f_{\mathrm{SS}}}{\sinh(k_{\mathrm{SS}} h)}, \tag{16}$$

where $H_{\mathrm{SS,rms}}$ is the root-mean-square SS wave height, and f_{SS} and k_{SS} are the mean wave frequency and wavenumber for SS waves. Likewise, U_{IG} at the bottom is computed using linear wave theory for a free shallow-water wave,

$$U_{\mathrm{IG}} = \frac{H_{\mathrm{IG,rms}}}{2} \frac{2\pi f_{\mathrm{IG}}}{k_{\mathrm{IG}} h}, \tag{17}$$

where $H_{\mathrm{IG,rms}}$ is the root-mean-square IG wave height, and f_{IG} and k_{IG} are the mean wave frequency and wavenumber for IG waves. Solving for the energy dissipation factor f_e by applying the energy flux balance (Equation 13) along with Equations 5 and 15,

$$f_e = \frac{N_{\mathrm{IG}} - \frac{\partial F^+_{\mathrm{IG}}}{\partial x}}{\frac{0.8}{g} \langle U_{\mathrm{SS}} \rangle \langle U_{\mathrm{IG}} \rangle^2}. \tag{18}$$

The infragravity $0.8/g \langle U_{\mathrm{SS}} \rangle \langle U_{\mathrm{IG}} \rangle^2$ and $N_{\mathrm{IG}} - \partial F^+_{\mathrm{IG}}/\partial x$ for station pairs (P13, P11) and (P11, P08) are plotted as a function of time (Figure 11). The linear relationship between $N_{\mathrm{IG}} - \partial F^+_{\mathrm{IG}}/\partial x$ and $0.8/g \langle U_{\mathrm{SS}} \rangle \langle U_{\mathrm{IG}} \rangle^2$ results in $R^2 = 0.57$ and $R^2 = 0.69$ for (P13, P11) and (P11, P08). The amount of noise is consistent with instrument pairs considered appropriate for SS dissipation estimates; see Marques, Feddersen, MacMahan, Acevedo-Ramirez, and Suanda (2025) for more details. The bulk friction factor $\langle f_e \rangle$ for the two station pairs, estimated from the linear best fit, is 0.072 and 0.079, larger though comparable to Pomeroy et al. (2012) of 0.06 for a shallow-water (≈ 1.5 m) coral reef flat. The bulk friction factor $\langle f_e \rangle$ is also surprisingly similar to shallower (< 3.5 m) sandy shores of 0.08 as estimated by Henderson and Bowen (2002), though in shallow water for sandy shores, IG wave breaking (e.g., Battjes et al., 2004; Van Dongeren et al., 2007; de Bakker et al., 2014) and nonlinear transfers from IG to SS (e.g., Thomson et al., 2006; Henderson et al., 2006) also contribute, potentially influencing $\langle f_e \rangle$. Applying $\langle f_e \rangle$ to Eq. 15 multiplied by the density of seawater and the acceleration due to gravity, ρg, results in average dissipation $\overline{D}_{\mathrm{IG}}$ of 0.037 and 0.093 Wm^{-2}.

Estimates of IG bottom friction factor f_e are plotted as a function of $\langle A_{\mathrm{b,SS}} \rangle / \sigma_z^{\mathrm{ref}}$, where $\langle A_{\mathrm{b,SS}} \rangle$ is the spatially averaged SS bottom orbital excursion and σ_z^{ref} is the adopted site-average bottom roughness [0.9 m; (see Marques, Feddersen, MacMahan, Acevedo-Ramirez, & Suanda, 2025)] (Figure 12). A log-linear trend is observed between f_e and $\langle A_{\mathrm{b,SS}} \rangle / \sigma_z^{\mathrm{ref}}$, consistent with the empirical SS $f_e \approx \sigma_z / A_{\mathrm{b}}$ relationships by Thornton and MacMahan (2024) and Marques, Feddersen, MacMahan, Acevedo-Ramirez, and Suanda (2025), with scatter comparable to SS wave results. The consistency between IG and SS friction relationships underscores the role of seabed roughness in dissipating IG waves across rocky shores.

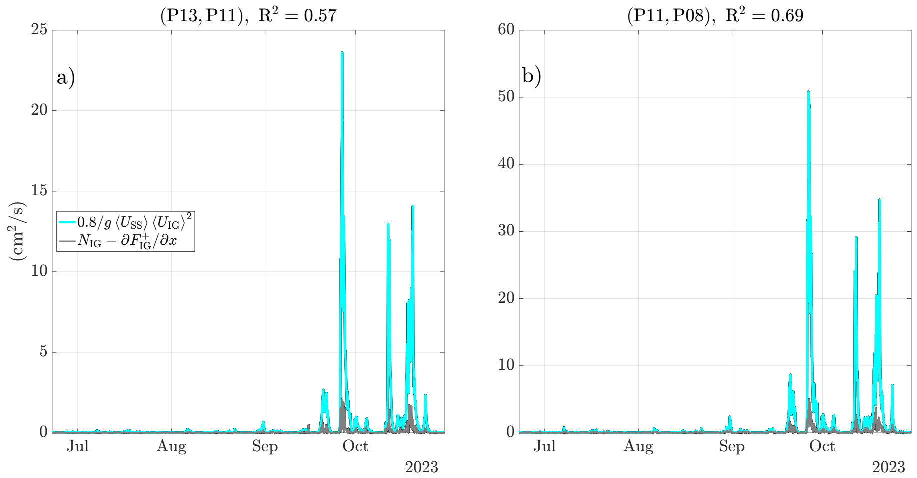

Figure 11. Infragravity $0.8/g \langle U_{\mathrm{SS}} \rangle \langle U_{\mathrm{IG}} \rangle^2$ (cyan line) and $N_{\mathrm{IG}} - \partial F^+_{\mathrm{IG}}/\partial x$ (gray line) for station pairs a) (P13, P11) and b) (P11, P08) versus time.

4.3 The Infragravity Waves at the Rocky Shores of China Rock

Infragravity wave energy at China Rock is evaluated by comparing the relative IG-to-SS energy with values reported for sandy beaches and coral reefs. This comparison uses the time-averaged ratio of IG energy at depth to nominal offshore SS energy, denoted as $\overline{E_{\mathrm{IG}}/E_{\mathrm{SS,o}}}$, and plotted as a function of nominal mean water depth (Figure 13). The ratio provides a generalized measure of the order of magnitude of IG energy across environments. Because $\overline{E_{\mathrm{IG}}/E_{\mathrm{SS,o}}}$ is often not directly reported in the literature, values were estimated from figures and tables. For example, graphical estimates from (Elgar et al., 1992) indicate that $\overline{E_{\mathrm{IG}}/E_{\mathrm{SS,o}}}$ is approximately 1% at 8 m depth at both Barber's Point, Hawaii, and Duck, NC, and less than 1% at Duck in 13 m depth. At Torrey Pines, CA, $\overline{E_{\mathrm{IG}}/E_{\mathrm{SS,o}}}$ was about 4% in 15 m depth based on (Thomson et al., 2006). For Terschelling, Netherlands, $\overline{E_{\mathrm{IG}}/E_{\mathrm{SS,o}}}$ was about 1% in 5 m depth, using $\mathrm{SS,o}$ from a wave buoy in 15 m depth, as estimated from (Ruessink, 1998). On coral reefs at Ningaloo Reef, Western Australia, the ratio is about 0.5% at a depth of 16 m (Pomeroy et al., 2012). In contrast, the present study at China Rock finds $\overline{E_{\mathrm{IG}}/E_{\mathrm{SS,o}}}$ to be approximately 0.2% in depths greater than 10 m, increasing linearly to about 0.5% at a depth of 7.5 m. These values are roughly an order of magnitude lower than those typically observed on sandy beaches.

In assessing the small IG energy at China Rock, it is helpful to highlight the study by Lange et al. (2024), who demonstrated that most IG energy on the inner shelf (depths in 10-15 m) along an extended reach of sandy shores is considered free, with only a small portion being bound. A large portion of free IG waves on sandy shores are those reflected at the shoreline, and most are refractively trapped (e.g., Herbers, Elgar, & Guza, 1995; Smit et al., 2018). Based on the analysis herein, rough rocky shores are primarily dissipative for IG waves; there is little to no reflection at the shoreline and, consequently,

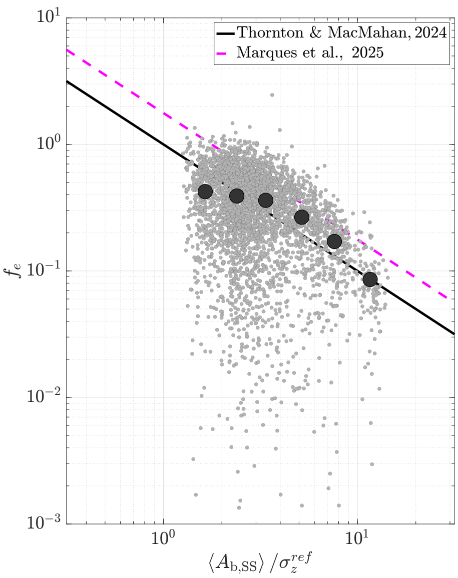

Figure 12. Friction factor estimates f_e, based on Equation 18, are plotted as a function of a $\langle A_{\mathrm{b,SS}} \rangle / \sigma_z^{ref}$, which is the non-dimensional ratios of spatially averaged SS bottom orbital excursions relative to the reference vertical standard deviation of the bottom elevation, where σ_z^{ref}=0.9 m. The larger circles represent the bin-averaged f_e estimates. The black and magenta lines depict the empirical f_e approximations based on SS waves by Thornton and MacMahan (2024) and Marques, Feddersen, MacMahan, Acevedo-Ramirez, and Suanda (2025).

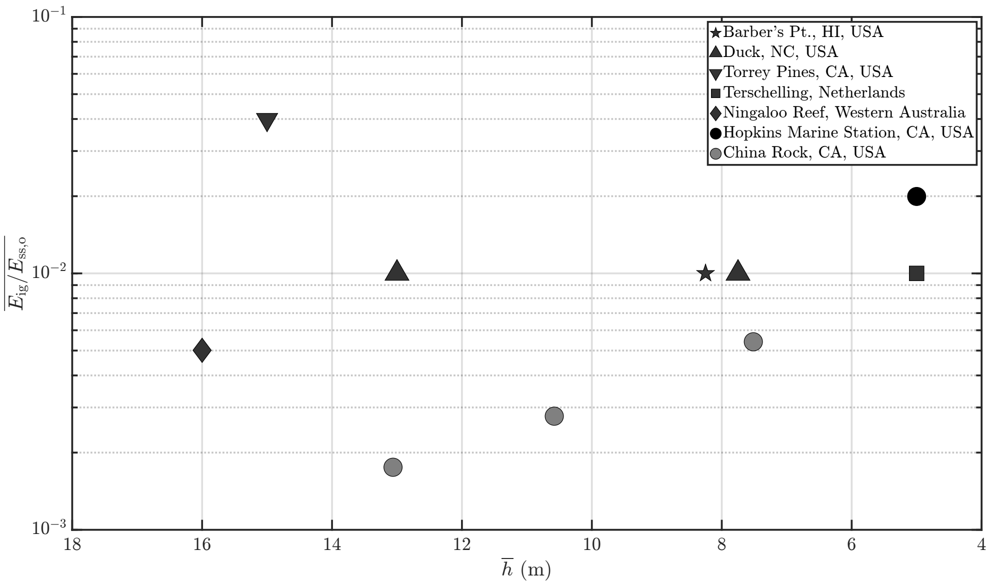

Figure 13. The relative infragravity-to-sea-swell energy $\overline{E_{\mathrm{IG}}/E_{\mathrm{SS,o}}}$ as a function of the nominal mean water depth $\overline{h}$ for various locations: Barber's Pt., HI, USA [★, black pentagon] (Elgar et al., 1992), Duck, NC, USA [▲, black triangle] (Elgar et al., 1992), Torrey Pines, CA, USA [▼, black downward triangle] (Thomson et al., 2006), Terschelling, Netherlands [■, black square] (Ruessink, 1998), Ningaloo Reef, Western Australia [⧫, black diamond] (Pomeroy et al., 2012), and Pacific Grove, CA, USA [●, black circle] data used from (Gon et al., 2020), and China Rock, CA, USA [●, gray circles].

no refractively trapped contributions. Therefore, there would be minimal additional IG waves other than those locally generated (shoreward propagating) by the SS waves through nonlinear interactions, as described above. China Rock, located on the western edge of the Monterey Peninsula, where much of the peninsula is primarily rocky, suggests that most IG energy dissipates around the peninsula (Figure 1). No additional local sources of free IG waves exist due to the extended reach of the predominant rocky shore. The closest sandy beaches capable of generating additional reflected and refractively trapped free IG waves are located at the base of the peninsula, relatively far from China Rock. These waves likely do not reach China Rock, which lies farther away along the outer edge of the peninsula. (Figure 1). Since there are no additional sources of IG waves at China Rock, and consistent with the analysis presented here, it suggests that IG waves on this rocky shore, which extends significantly alongshore, are locally generated by nonlinear interactions (e.g., Herbers & Burton, 1997; Norheim et al., 1998; Henderson et al., 2006; Thomson et al., 2006) by shoreward-propagating SS waves, with energy dissipated due to bottom friction. Nonlinear coupling is weaker on steep slopes (e.g., Herbers & Burton, 1997; Norheim et al., 1998), and bottom dissipation is found significant here, which suggests why the IG energy is relatively weaker at China Rock.

At a nearby small, complex rocky headland in Pacific Grove on the Monterey Bay side of the peninsula (see Fig. 1), specifically at Stanford's Hopkins Marine Station, $\overline{E_{\mathrm{IG}}/E_{\mathrm{SS,o}}}$ was estimated to be approximately 2% at 8 m depth (Figure 13), based on field data from Gon et al. (2020). Hopkins Marine Station is a rocky peninsula that extends approximately 200 m offshore and is about 300 m wide, beyond which the seafloor transitions to sand. In the shallow region ($<$ 2 m depth) of the rocky reef, IG waves are the dominant signal MacMahan et al. (2023), consistent with observations at other rocky headlands in $<$ 6 m depth Winter et al. (2017). Winter et al. (2017) reported standing IG waves in a mixed sandy and rocky coastal setting, where sandy areas likely served as sources of free, standing IG waves. Due to its proximity to adjacent sandy beaches (Figure 1), Hopkins Marine Station likely experiences enhanced free IG wave activity associated with standing-wave conditions (e.g., MacMahan et al., 2004; Reniers et al., 2006), resulting in IG energy levels more typical of sandy shore environments (Figure 13). In contrast, the rocky shoreline at China Rock is relatively alongshore-uniform over several kilometers, while the rocky coast near Hopkins shows significantly more variability, which influences IG wave behavior.

5 Conclusion

Field observations of infragravity (IG) waves on the inner shelf were conducted from June to October 2023 in water depths ranging from 8 to 13 m along the rough, steeper sloping (1:40) rocky shores off China Rock, Pebble Beach, CA. These observations capture summer and fall synoptic storm patterns, focusing on the analysis and comparison of IG wave behaviors in the cross-shore direction. The goal was to examine the influence of a rougher seabed and steeper bottom slopes on the inner shelf (seaward of sea-swell

(SS) breaking) and compare these findings to previous observations on sandy shores and coral reefs.

Similar to previous studies, integrated IG energy correlates with integrated SS energy and is locally related to offshore integrated IG energy. The spectral energy across the IG frequency band was surprisingly flat, showing only slight variation with tidal elevation or storm events. This pattern differs from prior sandy shore studies, particularly in the shallower water inner shelf region, where standing waves typically create nodal structure variations across frequencies in the energy density spectra. The IG energy per frequency correlates with the integrated SS energy, clearly defining the IG frequency limits to approximately 0.005 Hz and 0.04 Hz, consistent with previous findings.

The cross-spectral phase differences between instrument pairs were analyzed to investigate the cross-shore structure and propagation of IG waves. The results revealed a consistent pattern that varied minimally with tidal elevation and was relatively independent of fluctuations in SS energy. The spectral phase difference exhibited a sawtooth pattern, indicative of a progressive wave rather than the standing wave structure typically observed in shallow inner shelf sandy environments. Theoretical computations of spectral phase difference for a linear dispersive wave propagating in the cross-shore direction are consistent with the observations, suggesting that the IG waves are predominantly free. This conclusion was further supported by a normalized bispectral analysis, which estimated that only 10% of the energy was bound, remaining relatively consistent regardless of tidal elevation or SS energy, while 90% was considered free. The low percentage of bound wave energy corresponds with studies on sandy shores, although it is lower than most reported values.

A cross-shore energy flux balance between instrument pairs indicated that nonlinear energy transfer accounted for most of the cross-shore IG energy flux gradient, consistent with findings on sandy shores on the inner shelf. The nonlinear interactions surpassed the cross-shore IG energy flux gradient, particularly at the shallower station pair in water depths of 8 and 11 m. The surplus energy is balanced by the bottom dissipation, which is more pronounced over the rougher seabed of rocky shores and is generally deemed negligible for sandy shores. An analysis of friction factors for IG waves is comparable, though larger than those estimated on a shallow-water (≈ 1.5 m) coral reef flat. The friction factor trend correlates with previous studies on SS waves in rocky shore environments.

The relative IG-to-SS energy observed here was lower than that on sandy shores, coral reefs, and other rocky environments, likely due to the extended reach of the rocky shore, an effect that will be explored in future research. Assuming that the findings for the China Rock rocky shore are consistent across nearby rocky shores. The predominance of rocky shores over a long (8 km) stretch in this region would lack additional sources of free wave energy from IG wave reflection and correspondingly refractive-trapped waves, which are typical along extended stretches of sandy shores and have been hypothesized for mixed sandy and rocky shores. The results suggest that IG waves in this environment are locally generated and propagate freely toward the shore, where their energy is dissipated in shallower water, resulting in relatively minimal IG energy.

6 Open Research

The pressure time series data used in this study are available at the Zenodo dataset repository at https://doi.org/10.5281/zenodo.15857769 (MacMahan, 2025). Corresponding bathymetric data are available at the Zenodo dataset repository at https://doi.org/10.5281/zenodo.15199472 (Marques, Feddersen, & MacMahan, 2025), as presented in prior work by Marques, Feddersen, MacMahan, Acevedo-Ramirez, and Suanda (2025) and Quinn et al. (2025).

Acknowledgments

We thank the Naval Postgraduate School (NPS), Scripps Institute of Oceanography (SIO), and the University of North Carolina (UNC)-Chapel Hill, Oregon State University (OSU) field team members: for NPS– P. Jessen, M. Cook, C. Benbow, and the US Navy sailors; for SIO– B. Woodward, K. Smith, R. Grenzeback, L. Parry, S. Finnerty, and C. Black; for UNC-Chapel Hill– J. Rosman and A. Whipple, and for OSU– J. Marion. The seafloor mapping program at California State University at Monterey Bay, provided offshore bathymetry, and USGS LIDAR surveys provided topography. Monterey NOAA, CA Fish & Wildlife, CA State Lands, Pacific Grove, and Pebble Beach provided experimental permissions. We thank Chris Miller at NPS for his support with the permitting process. We thank the other ROXSI colleagues for fruitful conversations: J. Rosman, G. Wilson, A. Suanda, M. Denny, J. Kirby, M. Conlin, C. Acevedo, M. Malila, and K. Quinn. M. Cook is acknowledged for assistance with illustrations. This work was supported by ONR MURI: ROXSI–ROcky Shore eXperiments and SImulations [Grant #s N0001423WX00145 and N0001423WX01357 (MacMahan), N00014-21-1-2786 (Feddersen, Thornton, Marques)].

Appendix A Instrument Clock Differences

Long-term temporal gradients in $\Delta\alpha(f)$ are visible at P11 (Figure 6a) with the distinct yellow color edge for $\Delta\alpha = 180°$ that linearly increases as time progresses, starting at about $f = 0.04$ Hz and drifting to about $f = 0.06$ Hz by the experiment's end. A time difference $\Delta t(f)$ can be obtained from the phase difference $\Delta\alpha(f)$ by

$$\Delta t(f) = \frac{\Delta\alpha(f)}{360° f}. \tag{A1}$$

Using $\Delta\alpha(f) = 180°$ that starts at $f = 0.04$ Hz and linear drifts to $f = 0.06$ Hz from the beginning to the end of the experiment, the relative clock drift between sensors is calculated as,

$$\delta t_{\mathrm{r}} = \frac{\Delta\alpha(f_1)}{360° f_1} - \frac{\Delta\alpha(f_2)}{360° f_2} = \frac{180°}{360°\ 0.04\ \mathrm{Hz}} - \frac{180°}{360°\ 0.06\ \mathrm{Hz}} = 4.2\ \mathrm{s}. \tag{A2}$$

The relative clock drift δt_{r} indicates that this pair is small with a 4-second drift over 130 days, less than the specified absolute clock drifts of the RBR SoloD, estimated at an upper limit of 21 seconds over 130 days. The relative clock drift for the (P13, P08) is minimal. This conclusion assumes that the initial clock drifts early in the deployment are negligible and that these early $\Delta\alpha(f)$ patterns persist throughout the deployment, suggesting that timing errors are not a significant issue.

References

Aagaard, T., & Greenwood, B. (1994). Suspended sediment transport and the role of infragravity waves in a barred surf zone. *Marine Geology*, *118*(1–2), 23–48. doi: 10.1016/0025-3227(94)90111-2

Aagaard, T., & Greenwood, B. (2008). Infragravity wave contribution to surf zone sediment transport—the role of advection. *Marine Geology*, *251*(1–2), 1–14. doi: 10.1016/j.margeo.2008.01.017

Amador, A., Arzeno, I. B., Giddings, S. N., Merrifield, M. A., & Pawlak, G. (2020). Cross-shore structure of tidally driven alongshore flow over rough bathymetry. *J. Geophys. Res.: Oceans*, *125*, e2020JC016264. doi: 10.1029/2020JC016264

Ardhuin, F., Rawat, A., & Aucan, J. (2014). A numerical model for free infragravity waves: Definition and validation at regional and global scales. *Ocean Modelling*, *77*, 20–32. doi: 10.1016/j.ocemod.2014.02.006

Austin, J. A., & Lentz, S. J. (2002). The inner shelf response to wind-driven upwelling and downwelling. *Journal of Physical Oceanography*, *32*(7), 2171–2193. Retrieved from `https://doi.org/10.1175/1520-0485(2002)032<2171:TISRTW>2.0.CO;2` doi: 10.1175/1520-0485(2002)032⟨2171:TISRTW⟩2.0.CO;2

Baldock, T. E., Huntley, D. A., Bird, P. A. D., O'Hare, T., & Bullock, G. N. (2000). Breakpoint generated surf beat induced by bichromatic wave groups. *Coastal Engineering*, *39*, 213–242.

Battjes, J. A., Bakkenes, H. J., Janssen, T. T., & van Dongeren, A. R. (2004). Shoaling of subharmonic gravity waves. *Journal of Geophysical Research*, *109*(C2), C02009. doi: 10.1029/2003JC001863

Beach, R. A., & Sternberg, R. W. (1988). Suspended sediment transport in the surf zone: response to cross-shore infragravity motion. *Marine Geology*, *80*, 61–79.

Becker, J. M., Merrifield, M. A., & Yoon, H. (2016). Infragravity waves on fringing reefs in the tropical pacific: Dynamic setup. *Journal of Geophysical Research: Oceans*, *121*, 3010–3028. doi: 10.1002/2015JC011516

Benbow, C., & MacMahan, J. (2024). Observational insights of nearshore wind stress and parameterizations from gaussian process regressions. *Geophysical Research Letters*, *51*(19), e2023GL106825. doi: https://doi.org/10.1029/2023GL106825

Bertin, X., de Bakker, A., van Dongeren, A., Coco, G., Andr, G., & et al., F. A. (2018). Infragravity waves: From driving mechanisms to impacts. *Earth-Science Reviews*, *177*, 774–799. doi: 10.1016/j.earscirev.2018.01.002

Bird, E. (2011). *Coastal geomorphology: An introduction* (2nd ed.). West Sussex, England: John Wiley and Sons.

Brander, R. W., Kench, P. S., & Hart, D. (2004). Spatial and temporal variations in wave characteristics across a reef platform, warraber island, torres strait, australia. *Marine Geology*, *207*(1–4), 169–184. doi: 10.1016/j.margeo.2004.03.014

Collins, P., MacMahan, J., Thornton, E., Benbow, C., & Jessen, P. (2024). Beach and backward bragg sea-swell wave reflection across rocky and sandy shores. *Journal of Geophysical Research: Oceans*, *129*, e2023JC020177. doi: 10.1029/2023JC020177

Contardo, S., Lowe, R. J., Hansen, J. E., Rijnsdorp, D. P., Dufois, F., & Symonds, G. (2021). Free and forced components of shoaling long waves in the absence of short-wave breaking. *Journal of Physical Oceanography*, *51*(5), 1465-1487.

Retrieved from https://journals.ametsoc.org/view/journals/phoc/51/5/JPO-D-20-0214.1.xml doi: 10.1175/JPO-D-20-0214.1

de Bakker, A., Brinkkemper, J., Steen, F. V. D., Tissier, M., & Ruessink, B. (2016). Cross-shore sand transport by infragravity waves as a function of beach steepness: Sand transport by infragravity waves. *Journal of Geophysical Research: Earth Surface*, *121*(10), 1786–1799. doi: 10.1002/2016JF003878

de Bakker, A., Tissier, M., & Ruessink, B. (2014). Shoreline dissipation of infragravity waves. *Continental Shelf Research*, *72*, 73–82. doi: 10.1016/j.csr.2013.11.013

de Bakker, A., Tissier, M., & Ruessink, B. (2016). Beach steepness effects on nonlinear infragravity-wave interactions: A numerical study. *Journal of Geophysical Research: Oceans*, *121*, 554–570. doi: 10.1002/2015JC011268

Elgar, S., & Guza, R. T. (1985). Observations of bispectra of shoaling surface gravity waves. *Journal of Fluid Mechanics*, *161*, 425–448. doi: 10.1017/S0022112085003037

Elgar, S., Herbers, T. H. C., Okihiro, M., Oltman-Shay, J., & Guza, R. T. (1992). Observations of infragravity waves. *Journal of Geophysical Research*, *97*(C10), 15573–15577.

Feddersen, F., Marques, O. B., MacMahan, J. H., & Grenzeback, R. L. (2024). Estimating directional wave spectra properties in nonbreaking waves from a uas-mounted multibeam lidar. *Journal of Atmospheric and Oceanic Technology*, *41*(5), 515 - 530. Retrieved from https://journals.ametsoc.org/view/journals/atot/41/5/JTECH-D-23-0129.1.xml doi: 10.1175/JTECH-D-23-0129.1

Fiedler, J. W., Smit, P. B., Brodie, K. L., McNinch, J., & Guza, R. (2019). The offshore boundary condition in surf zone modeling. *Coastal Engineering*, *143*, 12–20. Retrieved from https://doi.org/10.1016/j.coastaleng.2018.10.014 doi: 10.1016/j.coastaleng.2018.10.014

Gon, C. J., MacMahan, J. H., Thornton, E. B., & Denny, M. (2020). Wave dissipation by bathymetry friction on the inner shelf of a rocky shore. *J. Geophys. Res: Oceans*, *125*(e2019JC015963). doi: 10.1029/2019JC015963

Guza, R. T., & Thornton, E. B. (1980). Local and shoaled comparisons of sea surface elevations, pressures, and velocities. *Journal of Geophysical Research*, *85*(C3), 1524–1530. doi: 10.1029/JC085iC03p01524

Guza, R. T., & Thornton, E. B. (1985). Observations of surf beat. *Journal of Geophysical Research*, *87*, 483–491.

Hardy, T. A., & Young, I. R. (1996). Field study of wave attenuation on an offshore coral reef. *Journal of Geophysical Research*, *101*(C6), 14311–14326. doi: 10.1029/96JC00202

Hasselmann, K. (1962). On the nonlinear energy transfer in a gravity-wave spectrum, 1, general theory. *Journal of Fluid Mechanics*, *12*, 481–500.

Haubrich, R. A. (1965). Earth noise, 5 to 500 millicycles per second: 1. spectral stationarity, normality, and nonlinearity. *Journal of Geophysical Research (1896-1977)*, *70*(6), 1415-1427. doi: https://doi.org/10.1029/JZ070i006p01415

Henderson, S. M., & Bowen, A. J. (2002). Observations of surf beat forcing and dissipation. *Journal of Geophysical Research*, *107*(C11), 3193. doi: 10.1029/2000JC000498

Henderson, S. M., Guza, R., Elgar, S., Herbers, T., & Bowen, A. J. (2006). Nonlinear generation and loss of infragravity wave energy. *Journal of Geophysical Research*, *111*, C12007. doi: 10.1029/2006JC003539

Hendrickson, J., & MacMahan, J. (2009). Diurnal sea breeze effects on inner-shelf cross-shore exchange. *Continental Shelf Research*, *29*(18), 2195-2206. doi: https://doi.org/10.1016/j.csr.2009.08.011

Herbers, T. H. C., & Burton, M. C. (1997). Nonlinear shoaling of directionally spread waves on a beach. *Journal of Geophysical Research*, *102*, 21101–21114.

Herbers, T. H. C., Elgar, S., & Guza, R. T. (1994). Infragravity-frequency (0.005–0.05 hz) motions on the shelf. part i: Forced waves. *Journal of Physical Oceanography*, *24*(5), 917–927. doi: 10.1175/1520-0485(1994)024⟨0917:IFHMOT⟩2.0.CO;2

Herbers, T. H. C., Elgar, S., & Guza, R. T. (1995). Generation and propagation of infragravity waves. *Journal of Geophysical Research*, *100*(C12), 24863. doi: 10.1029/95JC02680

Herbers, T. H. C., Elgar, S., Guza, R. T., & O'Reilly, W. C. (1995). Infragravity-frequency (0.005–0.05 hz) motions on the shelf. part ii: Free waves. *Journal of Physical Oceanography*, *25*(6), 1063–1079. doi: 10.1175/1520-0485(1995)025⟨1063:IFHMOT⟩2.0.CO;2

Hlywiak, J., Flagg, D., Hong, X., Doyle, J., Benbow, C., Curcic, M., … Williams, N. (2023). Evaluation of atmospheric surface layer flux parameterization within the coastal regime. *Bulletin of the American Meteorological Society*. doi: 10.1175/MWR-D-22-0303.1

Huntley, D. A. (1976). Long-period waves on a natural beach. *Journal of Geophysical Research*, *81*, 6441–6449.

Huntley, D. A., Guza, R. T., & Thornton, E. B. (1981). Field observations of surf beat: 1. progressive edge waves. *Journal of Geophysical Research*, *86*(C7), 6451–6466. doi: 10.1029/JC086iC07p06451

Inch, K., Davidson, M., Masselink, G., & Russell, P. (2017). Observations of nearshore infragravity wave dynamics under high energy swell and wind-wave conditions. *Continental Shelf Research*, *138*, 19–31. doi: 10.1016/j.csr.2017.02.010

Janssen, T. T., Battjes, J. A., & Dongeren, A. R. V. (2003). Long waves induced by short-wave groups over a sloping bottom. *Journal of Geophysical Research*, *108*(C8), 3252. doi: 10.1029/2002JC001515

Kim, J., & Powers, E. J. (1979). Digital bispectral analysis and its applications. *IEEE Transactions on Acoustics, Speech, and Signal Processing*, *27*(2), 120–132. doi: 10.1109/TASSP.1979.1163209

Lange, A. M. Z., Fiedler, J. W., Merrifield, M. A., & Guza, R. T. (2024). Free infragravity waves on the inner shelf: Observations and parameterizations at two southern california beaches. *Journal of Geophysical Research: Oceans*, *129*, e2023JC020378. doi: 10.1029/2023JC020378

Lentz, S. J., & Fewings, M. R. (2012). The wind- and wave-driven inner-shelf circulation. *Annual Review of Marine Science*, *4*(1), 317–343. Retrieved from `https://doi.org/10.1146/annurev-marine-120709-142745` doi: 10.1146/annurev-marine-120709-142745

Longuet-Higgins, M. S., & Stewart, R. W. (1962). Radiation stress and mass transport in gravity waves, with application to 'surf beats'. *Journal of Fluid Mechanics*, *13*(4), 481–504. doi: 10.1017/S0022112062000877

Lugo-Fernandez, A., Roberts, H. H., Jr., W. J. W., & Carter, B. L. (1998). Water level and currents of tidal and infra gravity periods at tague reef, st. croix (usvi). *Coral Reefs*, *17*, 343–349.

MacMahan, J. H. (2015). Low-frequency seiche in a large bay. *Journal of Physical Oceanography*, *45*(3), 716–723. doi: 10.1175/JPO-D-14-0169.1

MacMahan, J. H. (2025). *Roxsi pressure dataset for china rock 2023.* Retrieved from `https://doi.org/10.5281/zenodo.15857769` (Zenodo, accessed 10 July 2025)

MacMahan, J. H., Reniers, A. J. H. M., Thornton, E. B., & Stanton, T. (2004). Infragravity rip current pulsations. *Journal of Geophysical Research*, *109*. Retrieved from `http://dx.doi.org/10.1029/2003JC002068` doi: 10.1029/2003JC002068

MacMahan, J. H., Thornton, E. B., Dressel, S., & Cook, M. (2024). Intermediate wave scale rocky bottom variability for the nearshore along california. *Earth* *and Space Science*, *11*, e2023EA003475. Retrieved from https://doi.org/10.1029/2023EA003475 doi: 10.1029/2023EA003475

MacMahan, J. H., Thornton, E. B., Patria, N., Gon, C., & Denny, M. (2023). Rip currents off rocky-shore surge channels. *Journal of Geophysical Research: Oceans*, *128*(8), e2022JC019317. doi: https://doi.org/10.1029/2022JC019317

Marques, O. B., Feddersen, F., & MacMahan, J. H. (2024). An effective water depth correction for pressure-based wave statistics on rough bathymetry. *Journal of Atmospheric and Oceanic Technology*, *41*(11), 1047–1062. doi: 10.1175/JTECH-D-23-0118.1

Marques, O. B., Feddersen, F., & MacMahan, J. H. (2025). *Dataset for observations of wave energy dissipation by bottom friction on rocky shores.* Retrieved from https://doi.org/10.5281/zenodo.15199472 (Dataset, accessed 11 April 2025)

Marques, O. B., Feddersen, F., MacMahan, J. H., Acevedo-Ramirez, C. A., & Suanda, S. H. (2025). Observations of wave energy dissipation by bottom friction on rocky shores. *Journal of Physical Oceanography*, *55*, 593–610. doi: 10.1175/JPO-D-24-0144.1

Martins, K. (2024). *Bispectral analysis.* Retrieved from https://github.com/ke-martins/bispectral-analysis (GitHub repository)

Martins, K., Bonneton, P., de Viron, O., Turner, I., Harley, M., & Splinter, K. (2023). New perspectives for nonlinear depth-inversion of the nearshore using boussinesq theory. *Geophysical Research Letters*, *50*(2), e2022GL100498. doi: 10.1029/2022GL100498

Martins, K., Bonneton, P., Lannes, D., & Michallet, H. (2021). Relation between orbital velocities, pressure, and surface elevation in nonlinear nearshore water waves. *Journal of Physical Oceanography*, *51*(11), 3539–3556. doi: 10.1175/JPO-D-21-0061.1

Martins, K., Bonneton, P., & Michallet, H. (2021). Dispersive characteristics of non-linear waves propagating and breaking over a mildly sloping laboratory beach. *Coastal Engineering*, *167*, 103917. doi: 10.1016/j.coastaleng.2021.103917

Monismith, S. G., Rogers, J. S., Koweek, D., & Dunbar, R. B. (2015). Frictional wave dissipation on a remarkably rough reef. *Geophysical Research Letters*, *42*, 4063–4071. doi: 10.1002/2015GL063804

Mulligan, R. P., Hay, A. E., & Bowen, A. J. (2010). A wave driven jet over a rocky shoal. *J. Geophys. Res: Oceans*, *115*(C10038). doi: 10.1029/2009JC006027

Nakaza, E., & Hino, M. (1991). Bore-like surf beat in a reef zone caused by wave groups of incident short period waves. *Fluid Dynamics Research*, *7*, 89. doi: 10.1016/0169-5983(91)90062-N

Nidzieko, N. (2010). Tidal asymmetry in estuaries with mixed semidiurnal/diurnal tides. *Journal of Geophysical Research*, *115*. doi: 10.1029/2009JC005864

Norheim, C., Herbers, T., & Elgar, S. (1998). Nonlinear evolution of surface wave spectra on a beach. *Journal of Physical Oceanography*, *28*, 1534–1551.

Okihiro, M., Guza, R. T., & Seymour, R. J. (1993). Excitation of seiche observed in a small harbor. *Journal of Geophysical Research*, *98*, 18201–18211.

Oltman-Shay, J., & Howd, P. A. (1993). Edge waves on nonplanar bathymetry and alongshore currents: a model and data comparison. *Journal of Geophysical Research*, *98*, 2495–2507.

Pequignet, A.-C. N., Becker, J. M., & Merrifield, M. A. (2014). Energy transfer between wind waves and low-frequency oscillations on a fringing reef, ipan, guam. *Journal of Geophysical Research: Oceans*, *119*, 6709–6724. doi: 10.1002/2014JC010179

Pequignet, A.-C. N., Becker, J. M., Merrifield, M. A., & Aucan, J. (2009). Forcing of resonant modes on a fringing reef during tropical storm man-yi. *Geophysical Research Letters*, *36*, L03607. doi: 10.1029/2008GL036259

Poate, T., Masselink, G., Austin, M. J., Dickson, M., & McCall, R. (2018). The role of bed roughness in wave transformation across sloping rock shore platforms. *J. Geophys. Res: Earth Surface*, *123*(1), 97–123. doi: 10.1002/2017JF004277

Poate, T., Masselink, G., Austin, M. J., Inch, K., Dickson, M., & McCall, R. (2020). Infragravity wave generation on shore platforms: Bound long wave versus breakpoint forcing. *Geomorphology*, *350*, 106880. doi: 10.1016/J.GEOMORPH.2019.106880

Pomeroy, A., Lowe, R., Symonds, G., Dongeren, A. V., & Moore, C. (2012). The dynamics of infragravity wave transformation over a fringing reef. *Journal of Geophysical Research*, *117*, C11022. doi: 10.1029/2012JC008310

Quinn, K. J., Feddersen, F., Marques, O. B., MacMahan, J. H., & Suanda, S. H. (2025). Depth-averaged subtidal and tidal circulation off of a rocky shore. *Journal of Geophysical Research: Oceans*, *130*, e2024JC022047. Retrieved from `https://doi.org/10.1029/2024JC022047` doi: 10.1029/2024JC022047

Reniers, A., MacMahan, J., Thornton, E. B., & Stanton, T. P. (2006). Modelling infragravity motions on a rip-channeled beach. *Coastal Engineering*, *53*, 209–222. Retrieved from `https://doi.org/10.1016/j.coastaleng.2005.10.010` doi: 10.1016/j.coastaleng.2005.10.010

Reniers, A., Naporowski, R., Tissier, M. F. S., de Schipper, M. A., Akrish, G., & Rijnsdorp, D. P. (2021). North sea infragravity wave observations. *Journal of Marine Science and Engineering*, *9*(2), 141. Retrieved from `https://doi.org/10.3390/jmse9020141` doi: 10.3390/jmse9020141

Reniers, A., Roelvink, J. A., & Thornton, E. B. (2004). Morphodynamic modeling of an embayed beach under wave group forcing. *Journal of Geophysical Research*, *109*. doi: 10.1029/2002JC001586

Rijnsdorp, D. P., Smit, P. B., & Guza, R. T. (2022). A nonlinear, non-dispersive energy balance for surfzone waves: infragravity wave dynamics on a sloping beach. *Journal of Fluid Mechanics*, *944*, A45. Retrieved from `https://doi.org/10.1017/jfm.2022.512` doi: 10.1017/jfm.2022.512

Roelvink, J. A., & Reniers, A. J. H. M. (2012). *A guide to modelling coastal morphology.* Singapore: World Scientific.

Ruessink, B. (1998). Bound and free infragravity waves in the nearshore zone under breaking and nonbreaking conditions. *Journal of Geophysical Research: Oceans*, *103*(C6), 12795–12805.

Ruju, A., Lara, J., & Losada, I. (2012). Radiation stress and low-frequency energy balance within the surf zone: a numerical approach. *Coast. Eng.*, *68*, 44–55.

Sheremet, A., Guza, R. T., Elgar, S., & Herbers, T. H. C. (2002). Observations of nearshore infragravity waves: Seaward and shoreward propagating components. *Journal of Geophysical Research*, *107*(C8), 3095. doi: 10.1029/2001JC000970

Smit, P. B., Janssen, T. T., Herbers, T. H. C., Taira, T., & Romanowicz, B. A. (2018). Infragravity wave radiation across the shelf break. *Journal of Geophysical Research: Oceans*, *123*, 4483–4490. doi: 10.1029/2018JC013986

Sous, D., Martins, K., Tissier, M., Bouchette, F., & Meulé, S. (2023). Spectral wave dissipation over a roughness-varying barrier reef. *Geophysical Research Letters*, *50*, e2022GL102104. doi: 10.1029/2022GL102104

Suhayda, J. N. (1974). Standing waves on beaches. *Journal of Geophysical Research*, *79*, 3065–3071.

Thomson, J., Elgar, S., Raubenheimer, B., Herbers, T. H. C., & Guza, R. T. (2006). Tidal modulation of infragravity waves via nonlinear energy losses in the surfzone. *Geophysical Research Letters*, *33*, L05601. doi: 10.1029/2005GL025514

Thornton, E. B., & Guza, R. T. (1983). Transformation of wave height distribution. *Journal of Geophysical Research*, *88*(C10), 5925–5938. doi: 10.1029/JC088iC10p05925

Thornton, E. B., & MacMahan, J. (2024). Update to friction factor formulations that impact rocky shores and coral reefs. *Journal of Geophysical Research: Oceans*, *129*, e2024JC021630. Retrieved from `https://doi.org/10.1029/`

2024JC021630 doi: 10.1029/2024JC021630

Torres-Freyermuth, A., Marino-Tapia, I., Coronado, C., Salles, P., Medellin, G., Pedrozo-Acuna, A., ... Iglesias-Prieto, R. (2012). Wave-induced extreme water levels in the puerto morelos fringing reef lagoon. *Natural Hazards and Earth System Sciences*, *12*, 3765–3773.

Van Dongeren, A., Battjes, J., Janssen, T., van Noorloos, J., Steenhauer, K., Steenbergen, G., & Reniers, A. (2007). Shoaling and shoreline dissipation of low-frequency waves. *Journal of Geophysical Research*, *112*, C02011. doi: 10.1029/2006JC003701

Winter, G., Lowe, R. J., Symonds, G., Hansen, J. E., & van Dongeren, A. R. (2017). Standing infragravity waves over an alongshore irregular rocky bathymetry. *Journal of Geophysical Research: Oceans*, *122*, 4868–4885. doi: 10.1002/2016JC012242

Xu, J. P. (1999). Local wave climate and long-term bed shear stress characteristics in monterey bay, california. *Marine Geology*, *159*, 341–353. doi: 10.1016/S0025-3227(98)00192-3